國立臺灣大學理學院物理學研究所

博士論文

Department of Physics
College of Science
National Taiwan University
Doctoral Dissertation

基於囚禁離子系統中的腔體量子電動力學

Cavity QED simulation with a trapped ion system

李鎮宇
Chen-Yu Lee

指導教授：林俊達 博士
Advisor: Guin-Dar Lin, Ph.D.

中華民國 112 年 7 月
July 2023

doi:10.6342/NTU202301896

doi:10.6342/NTU202301896

國立臺灣大學博士學位論文
口試委員會審定書
PhD DISSERTATION ACCEPTANCE CERTIFICATE
NATIONAL TAIWAN UNIVERSITY

（論文中文題目）(Chinese title of PhD dissertation)

基於囚禁離子系統中的腔體量子電動力學

（論文英文題目）(English title of PhD dissertation)

Cavity QED simulation with a trapped ion system

本論文係 李鎮宇 (姓名) D05222008 （學號）在國立臺灣大學 物理學系 (系/所/學位學程)完成之博士學位論文，於民國 112 年 7 月 11 日承下列考試委員審查通過及口試及格，特此證明。

The undersigned, appointed by the Department / Institute of Physics on 11 (date) 7 (month) 2023 (year) have examined a PhD dissertation entitled above presented by Chen-Yu Lee (name) D05222008 (student ID) candidate and hereby certify that it is worthy of acceptance.

口試委員 Oral examination committee:

林俊達	張銘顯	管希聖
（指導教授 Advisor）		
童世光	王冠堂	仇祥華

系主任/所長 Director:

doi:10.6342/NTU202301896

doi:10.6342/NTU202301896

致謝

尊敬的指導教授、各位評審委員、親愛的家人、朋友與研究室夥伴：

時光荏苒，轉眼間，我的論文即將完成，這是我學術生涯中的一個重要里程碑。在這特別的時刻，我要向所有支持、指導、鼓勵過我的人表示最衷心的感謝。

首先，我要感謝我的指導教授 林俊達。您在這段研究之旅中給予我無微不至的指導和支持，不僅在學術上給予我許多寶貴的建議，還在生活中給予我無盡的鼓勵。您的悉心指導讓我更深入地了解專業知識，培養了我的研究能力和解決問題的勇氣。您是我學習和成長的重要靈魂導師，在此我深深地感謝您。

感謝各位評審委員，感謝您們在百忙之中抽出寶貴的時間閱讀、評價我的論文。您們的寶貴意見和建議對我的論文進行了重要的完善和提升，讓我深感受益良多。

感謝我的家人，感謝你們無條件的愛和支持。在這段學術探索的過程中，你們總是在背後默默支持著我，給予我溫暖的擁抱和勇氣。你們是我最堅實的後盾，我永遠感激你們。

感謝我的朋友和研究室夥伴們（林冠廷、許婷、沈于晴、詹資莘、方文瀚、吳鈞季、林宥成、曹以琳、劉鎮瑜），你們是我生活中的陪伴者和知己。在學業和生活的道路上，我們攜手成長，互相鼓勵，無數次的交流和討論使我受益良多，讓我更加充實和堅定地朝著目標前進。特別要感謝林冠廷學長，沒有您在我博士一年級時推薦進入林俊達教授的研究室，我可能至今都不知道會過怎樣挑戰的生活。

最後，我要感謝所有曾經在我生活中出現過的人，無論你是否知曉，都是我成長路上的一部分。每個人都在我心中留下了深深的印記，給予我無限的啓發和動

doi:10.6342/NTU202301896

力。

感謝你們每一位，是你們的支持與陪伴，讓我堅持走到了論文完成的這一刻。我將繼續保持學習的熱情，持續追求知識與進步，爲社會的發展盡一份微薄之力。

謝謝大家！

doi:10.6342/NTU202301896

摘要

本研究旨在探討使用光鑷在大型離子晶體中操作聲子自由度的理論研究。我們的方法是利用光鑷選擇性地固定特定離子，創造出阻礙聲波傳播的屏障。這樣一來，我們可以模擬一維聲腔，其中這些屏障之間的一部分離子對有效腔體的局部運動模式做出貢獻。

爲了瞭解腔體的特性，我們計算了模態頻譜、損耗率和馬可夫性。根據我們對這些模式施加藍邊帶或紅邊帶躍遷，我們可以將腔體模態激發或阻抑。在激發的情況下，我們觀察到聲子雷射行爲，包括雷射閾值的出現、接近泊松分佈的統計特性、相干性、線寬窄化，以及引人入勝的效應，如模式競爭和多穩定性。另一方面，在阻抑的情況下，我們發現某些次都卜勒冷卻（電磁誘發透明冷卻）技術仍適用於局部模式。因此，與不使用光鉗的情況相比，可以更有效且節省成本地冷卻子陣列。

我們提出的系統爲研究腔體量子電動力學提供了聲學類比，爲聲子媒介的量子操作、通信和計算開創了道路。

中文關鍵字: 囚禁離子、光學鑷子、聲子雷射、模式競爭、電磁誘發透明冷卻

doi:10.6342/NTU202301896

doi:10.6342/NTU202301896

Abstract

In this study, we propose a theoretical investigation into the manipulation of phononic degrees of freedom using optical tweezers in a large ionic crystal. Our approach involves the use of optical tweezers to selectively immobilize specific ions, creating barriers that impede the propagation of acoustic waves. By doing so, we can emulate a one-dimensional acoustic cavity, where a subset of ions between these barriers contributes to the local motional modes of the effective cavity.

To gain insights into the characteristics of the cavity, we calculate the mode spectrum, loss rates, and the Markovianity of the cavity. Depending on whether we apply blue or red sideband transitions to these modes, we can either pump or damp the cavity mode excitations. In the case of pumping, we observe phonon lasing behavior, including the emergence of lasing thresholds, near-Poisson statistics, correlations, line-narrowing, as well as intriguing effects such as mode competition and multi-stability. On the other hand, in the case of damping, we discover that certain sub-Doppler cooling (electromagnetically-induced-transparency cooling) techniques remain applicable to the local modes. Consequently, the sub-array can be cooled more efficiently and economically compared to scenarios without the use of tweezers.

Our proposed system provides an acoustic equivalent for exploring cavity quantum electrodynamics, opening up possibilities for quantum manipulation, communication, and computation mediated by phonons.

Keywords: trapped ion, optical tweezers, phonon lasers, mode competition, EIT cooling

doi:10.6342/NTU202301896

doi:10.6342/NTU202301896

Contents

doi:10.6342/NTU202301896

doi:10.6342/NTU202301896

doi:10.6342/NTU202301896

doi:10.6342/NTU202301896

List of Figures

doi:10.6342/NTU202301896

doi:10.6342/NTU202301896

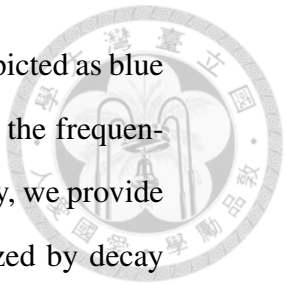

doi:10.6342/NTU202301896

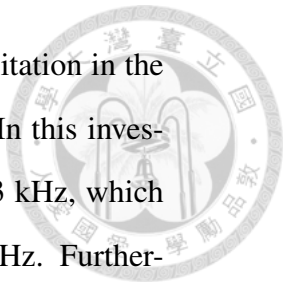

doi:10.6342/NTU202301896

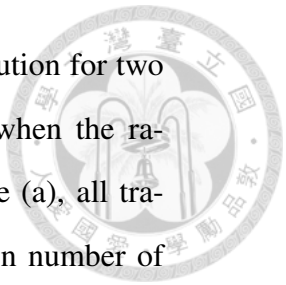

doi:10.6342/NTU202301896

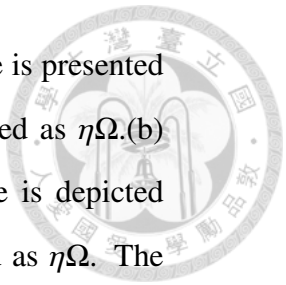

doi:10.6342/NTU202301896

doi:10.6342/NTU202301896

doi:10.6342/NTU202301896

List of Tables

doi:10.6342/NTU202301896

doi:10.6342/NTU202301896

Chapter 1

Introduction

1.1 Motivation

"*Nature isn't classical, dammit, and if you want to make a simulation of nature, you'd better make it quantum mechanical, and by golly it's a wonderful problem because it doesn't look so easy.*" — Richard Feynman, 1965 Nobel Prize laureate.

Inspired by this perspective, for the past decades scientists have actively pursued and achieved quantum simulation using various physical systems, including trapped ions, cold atoms, superconducting loops, among others. Among these systems, trapped-ion systems have emerged as highly promising for quantum information processing (QIP) [3, 4]. They offer several advantages that contribute to their appeal. Firstly, trapped ions possess a universal coherence time [5] and exhibit exceptional fidelity [6, 7] in executing operations on ion qubits. Moreover, the individual ion qubits can be precisely controlled and manipulated due to their identical properties, further enhancing their utility. Notably, the high connectivity of trapped-ion QIP surpasses that of other platforms, enabling the implementation of complex quantum algorithms and efficient information processing.

In addition to the aforementioned advantages, it is important to recognize the significance of phonon motion in trapped-ion systems. The Hilbert space associated with phonons is considerably larger than that of two-level systems when considering an equal number of ions. This implies that phonons offer distinct advantages in quantum simulations, which should not be overlooked. Therefore, considering and harnessing the poten-

doi:10.6342/NTU202301896

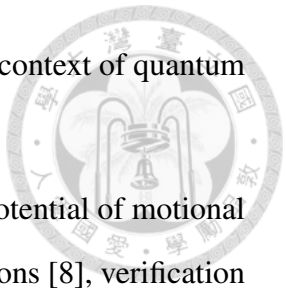

tial of phonons can provide valuable insights and opportunities in the context of quantum simulations.

In recent years, some research groups have begun to explore the potential of motional degrees of freedom, utilizing them for tasks such as arithmetic operations [8], verification of the quantum Jarzynski equality [9], preparation of phononic quantum gates [10], and the development of phonon lasers [11, 12, 13].

The successful realization of the first phonon laser in a trapped-ion system marked a significant milestone, with optical forces playing a key role in its achievement. [11]. In this system, a single ion displayed self-sustained oscillation beyond a specific threshold, absorbing energy from optical sources to maintain the oscillation. Thereafter, researchers have explored and implemented various proposals in trapped-ion systems [12, 13], quantum dots [14, 15, 16], and optomechanical systems [16, 17, 18, 19, 20, 21, 22, 23, 24, 25]. Phononic systems have exhibited intriguing properties analogous to conventional lasers, including oscillation thresholds [11, 17, 19, 20, 22, 24, 25, 26], Poissonian distributions [24], linewidth narrowing [17, 18, 19, 22, 24, 26], injection locking [12, 13], and mode competition [20, 25]. However, many of these schemes necessitate complex architectural designs that are not easily scalable to incorporate additional motional modes. Furthermore, the parameters of the lasing resonator are typically predetermined during fabrication, limiting exploration of the rich physics underlying phonons.

In order to achieve quantum simulation, cooling to the motional ground state is important. Therefore, in this dissertation we have revealed that certain sub-Doppler cooling techniques remain applicable to the local modes, even in the presence of optical tweezers. This observation has significant implications, as it enables more efficient and cost-effective cooling of the sub-array compared to scenarios where tweezers are not employed. By leveraging these sub-Doppler cooling techniques, we can achieve enhanced control over the temperature of the local modes, leading to improved stability and coherence in the trapped-ion system. This finding highlights the potential for optimizing cooling strategies and underscores the practical advantages of incorporating optical tweezers into the experimental setup.

doi:10.6342/NTU202301896

Overall, the proposed system presents an acoustic analogue for investigating cavity quantum electrodynamics, opening avenues for phonon-mediated quantum manipulation, communication, and computation.

1.2 Ion trapping

In order to carry out ion-based experiments, it is crucial to trap the ions. To accomplish this, various techniques such as Paul traps, optical tweezers, and optical lattices have been utilized. In this section, we will summarize the operational principles of Paul traps and optical tweezers, as well as discuss some characteristics.

1.2.1 Ion traps

Earnshaw's theorem [27, 28] states that it is impossible to confine charged particles in a static electric field in a stable manner. Consequently, alternative methods must be employed to effectively trap charged particles such as ions. One such approach is the utilization of Paul traps [29]. As depicted in Figure 1.1 (a), a Paul trap consists of four electric rods. A pair of diagonal rods that are subjected to radial-frequency (RF) voltages can capture ions that move transversely in the x and y directions, while the remaining rods are segmented along the axial (z) direction with each piece supplied with different direct-current (DC) voltages to stabilize the axial motion of the particles in the z direction.

With advances in technology, ions can now be trapped on surfaces using a surface-electrode trap, as illustrated in Figure 1.1 (b) [30]. The trapping mechanism is similar to a Paul trap. By subjecting RF voltages to the two RF electrodes while keeping the center and outer electrodes at RF ground, electric pseudopotentials are generated. These pseudopotentials serve to confine the trapped ions in the radial directions. To regulate the longitudinal electric potentials, the outer electrodes are divided into segments. This segmentation allows for the control of the electric potentials along the axial direction, enabling the confinement of the trapped ions or their controlled movement in that direction.

For N ions on the surface-electrode trap, the potential including the Coulomb interac-

doi:10.6342/NTU202301896

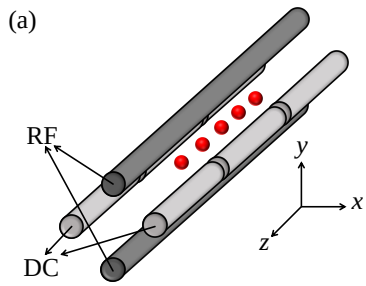

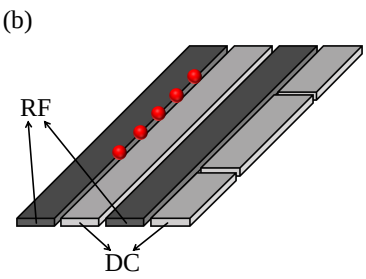

Figure 1.1: The schematic figure of an ion trap. (a) The standard linear RF Paul trap. (b) The surface-electrode trap.

tion reads

$$U = \sum_{i=1}^{N} \frac{1}{2} m \left(\omega_x^2 x_i^2 + \omega_y^2 y_i^2 \right) + \Phi(z_i) + \sum_{i<j} \frac{1}{4\pi\epsilon_0} \frac{e^2}{|\boldsymbol{r}_i - \boldsymbol{r}_j|}, \tag{1.2.1}$$

where m is the mass of the ion; ω_x and ω_y are the trapping frequencies along the x and y directions; e is the charge of a single ion; ϵ_0 is the vacuum permittivity; $\boldsymbol{r}_i = \{x_i, y_i, z_i\}$ is the position of the ith ion. The axial potential $\Phi(z_i)$ has a form [1]

$$\Phi(z_i) = \begin{cases} \frac{eV_{\mathrm{DC}}}{\pi} \left(\tan^{-1} \frac{h}{z_i + \frac{L}{2}} - \tan^{-1} \frac{h}{z_i - \frac{L}{2}} \right), & \text{for } |z_i| \leq \frac{L}{2} \\ \frac{eV_{\mathrm{DC}}}{\pi} \left(\tan^{-1} \frac{h}{z_i + \frac{L}{2}} - \tan^{-1} \frac{h}{z_i - \frac{L}{2}} + \pi \right), & \text{for } |z_i| > \frac{L}{2} \end{cases} \tag{1.2.2}$$

where $V_{\mathrm{DC}}\,(>0)$ is the voltage applied to the edge electrodes, h is the height of ions from the surface, and L is the distance between the edge electrodes. The equilibrium position z_i^0 of ith ions can be determined by minimizing the potential U. Figure 1.2 illustrates the equilibrium position z_i^0 with a unit d_0. We notice that the ion spacing get denser as the number of ions N increases (shown in the dashed line). For a small-scale system where the confining potential can be approximated as a harmonic one, the minimum ion separation obeys the relation $u_{min}(N) \approx \frac{2.018}{N^{0.559}}$ [31].

When an ion array is near the equilibrium position, we perform Taylor expansion and Eq. 1.2.1 has a form $U = \frac{1}{2} \sum_{i,j,\xi} A_{ij}^{\xi} \Delta x_i^{\xi} \Delta x_j^{\xi}$, where $\xi = x, y, z$ and the coupling matrix

doi:10.6342/NTU202301896

$A_{ij}^{\xi} = \left(\partial_{x_i^{\xi}} \partial_{x_i^{\xi}} U\right)\Big|_0$ is given by

$$A_{ij}^{\xi} = \begin{cases} m\omega_{\xi}^2 + \sum_{j=2}^{N} \sum_{i=1}^{j-1} \frac{e^2}{4\pi\epsilon_0} \frac{a_{\xi}}{\left|z_i^0 - z_j^0\right|^3}, & i = j \\ -\frac{e^2}{4\pi\epsilon_0} \frac{a_{\xi}}{\left|z_i^0 - z_j^0\right|^3}, & i \neq j \end{cases} \tag{1.2.3}$$

where $a_{x,y} = -1$ and $a_z = 2$ [32]. By diagonalizing the coupling matrix A_{ij}^{ξ}, it transforms the individual basis to the uncoupled collective basis. Figure 1.3 shows the mode frequencies for $N = 1 \sim 10$ with $\omega_{x,y} = 6\omega_0$, where $\omega_0 \equiv \sqrt{\frac{e^2}{md_0^3}}$. The center-of-mass mode has a lowest frequency in the axial direction. On the other hand, for the transverse direction, the highest frequency corresponds to the center-of-mass mode. It clearly displays that the spectral distribution of the transverse mode is narrower than the axial one.

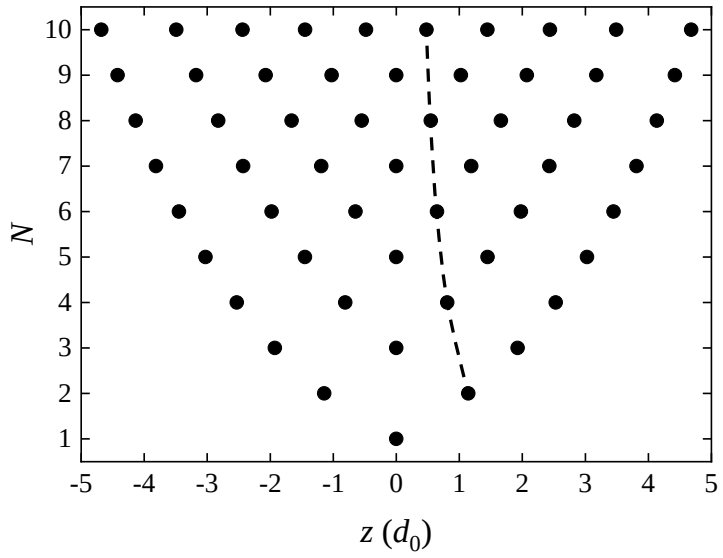

Figure 1.2: The equilibrium positions of N ions with a length unit d_0. The dashed line illustrates the ion separation gets narrower as number of ions increase.

1.2.2 Optical tweezers

Arthur Ashkin, the Nobel Prize laureate in Physics in 2018, made significant contributions to the development of optical tweezers [33]. Optical tweezers are specialized devices that utilize highly focused laser beams to generate forces capable of manipulating minuscule transparent objects. This technology enables the movement of cells or viral particles, the

doi:10.6342/NTU202301896

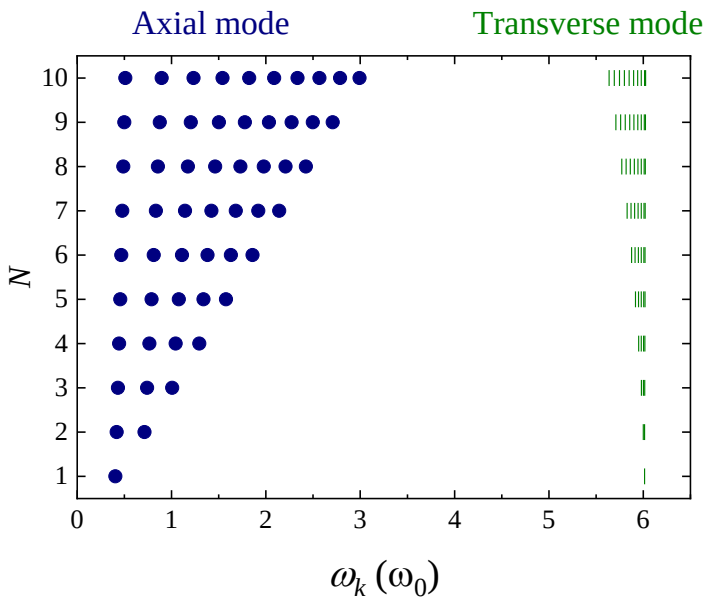

Figure 1.3: The eigenmode frequency of N ions with a frequency unit ω_0

deformation of cells into different shapes, and even the cooling of atoms. The precise and direct application of forces to cells and smaller targets has resulted in the widespread adoption of optical tweezers within the field of biology.

The principles underlying optical tweezers can be elucidated through two approaches: ray optics and the electric dipole approximation. When dealing with particles that possess diameters significantly larger than the wavelength of light, the trapping phenomenon can be adequately explained using ray optics. As a laser beam traverses an object, it undergoes refraction, altering its direction and momentum (Fig. 1.4 (a)). According to Newton's third law, the object experiences an equal and opposite change in momentum, resulting in a reaction force that ensures the conservation of total momentum within the system (Fig. 1.4 (b)). To achieve stable trapping of an object at the beam's center, a focused beam is required, where the central region contains a greater number of photons compared to the outer regions (Fig. 1.5 (a)). This discrepancy leads to a stronger force exerted on the object, compelling it towards the focal point (Fig. 1.5 (b)).

Conversely, when dealing with atomic systems where the trapped particle has a diameter considerably smaller than the wavelength of light, the conditions for Rayleigh scattering are met. In this scenario, the particle can be regarded as a point dipole within an inhomogeneous electromagnetic field. The dipole potential and scattering rate can be

doi:10.6342/NTU202301896

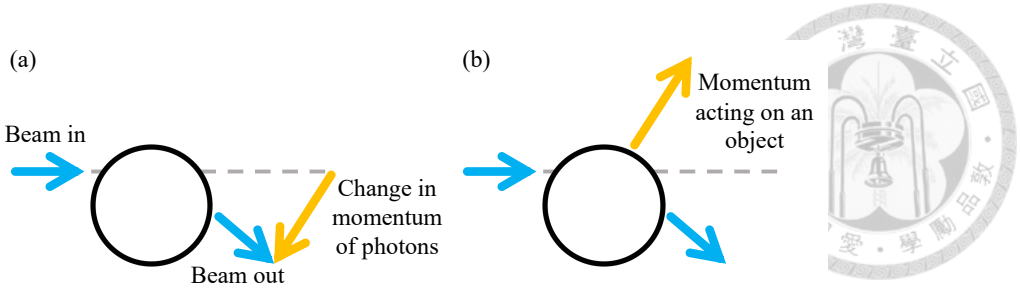

Figure 1.4: (a) The redirection of a light path and the alteration of momentum occur when light traverses an object with a high refractive index in the medium. (b)According to Newton's third law, an equal and opposite force is transferred from the photons to the object, resulting in a momentum change.

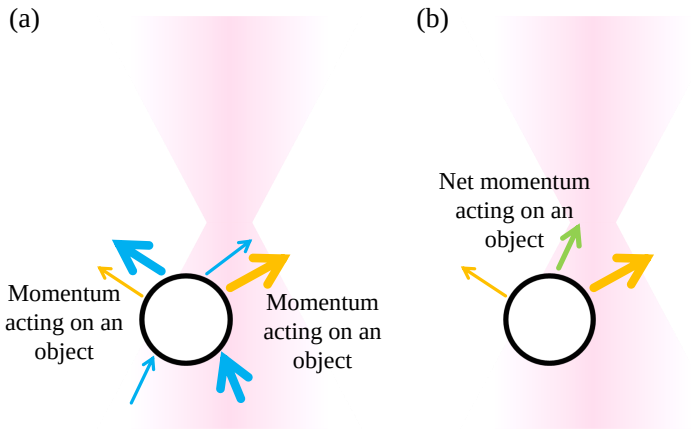

Figure 1.5: When two light paths pass through a dielectric micron-sized object, an interesting phenomenon arises. As a result of the light gradient, the path originating from the center of the beam carries a higher number of photons compared to the light path starting from the outer regions of the beam. Consequently, this uneven distribution of photons creates a stronger force that pulls the bead towards the focal point.

determined by applying the Lorentz force and the Lorentz oscillator model. Consequently, the dipole potential U_{dip} and scattering rate Γ_{sc} can be calculated as

$$U_{\text{dip}} = -\frac{2P}{\pi w^2}\sum_i \frac{3\pi c^2}{2\omega_0^3}\left(\frac{\gamma_i}{\omega_0-\omega_i}+\frac{\gamma_i}{\omega_0+\omega_i}\right), \tag{1.2.4}$$

$$\Gamma_{\text{sc}} = \frac{2P}{\pi w^2}\sum_i \frac{3\pi c^2}{2\hbar\omega_0^3}\left(\frac{\omega_i}{\omega_0}\right)^3\left(\frac{\gamma_i}{\omega_0-\omega_i}+\frac{\gamma_i}{\omega_0+\omega_i}\right)^2, \tag{1.2.5}$$

where $P, w, c, \gamma_i, \omega_0$, and ω_i are the incident laser power, the beam size, the speed of light, the natural linewidth for the ith atomic state, the incident laser frequency, and the transition frequency for the ith atomic state, respectively [34]. The strength of optical tweezers can be described by the equation $\sqrt{\frac{4U_{\text{dip}}}{mw^2}}$, where m denotes the mass of the atom.

doi:10.6342/NTU202301896

To illustrate this concept, we consider the $^{40}Ca^{+}$ ion 393 nm transition as an example (Fig. 1.6). Table 1.1 and 1.2 present the tweezers strengths and their corresponding scattering rates. These tables indicate that to increase the strength of the tweezers, the laser detuning ($\delta = \omega_0 - \omega_i$) of the laser and beam size should be reduced. However, a stronger tweezers strength leads to a higher scattering rate. Therefore, a trade-off between the tweezers strength and the scattering rate must be made.

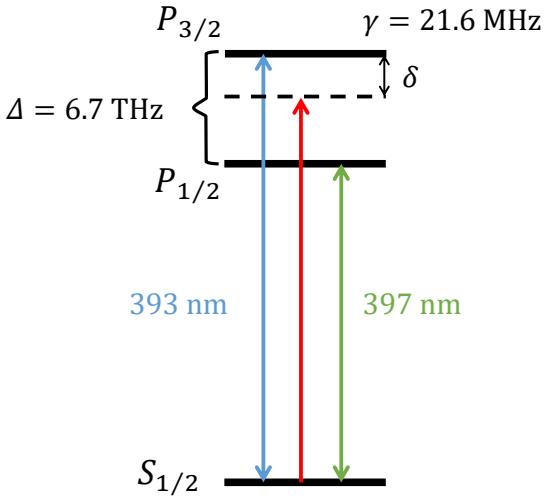

Figure 1.6: Atomic level configuration and relevant electric dipole transitions of $^{40}Ca^{+}$

Table 1.1: Tweezer strength ($2\pi \times$MHz)

w (μm)	δ ($2\pi \times$THz)		
	-10	-30	-50
0.6	12.9	5.64	4.24
0.7	9.52	4.14	3.12
0.8	7.29	3.17	2.39
0.9	5.76	2.51	1.89
1.0	4.67	2.03	1.53
1.1	3.86	1.68	1.26
1.2	3.24	1.41	1.06

$P = 100$ mW

doi:10.6342/NTU202301896

Table 1.2: Scattering rate Γ_{sc} (MHz)

w (μm)	δ ($2\pi \times$ THz)		
	-10	-30	-50
0.6	13.4	0.386	0.121
0.7	9.82	0.283	0.0888
0.8	7.52	0.217	0.0680
0.9	5.94	0.171	0.0537
1.0	4.81	0.139	0.0435
1.1	3.98	0.115	0.0360
1.2	3.34	0.0964	0.0302

$P = 100$ mW

1.3 Phonon laser

1.3.1 Overview

The term "laser" stands for "light amplification by the stimulated emission of radiation," and its underlying principle was first proposed by Albert Einstein in 1917 [35]. The first laser was constructed approximately 50 years after Einstein's proposal [36], as a result of a self-organizing process whereby a collection of emissions becomes synchronized to produce identical light particles (photons). As a consequence of this synchronization, lasers exhibit unique properties, including monochromaticity, coherence, and directionality. Interestingly, a similar phenomenon of self-organized synchronization can give rise to the generation of coherent vibrations, known as a phonon laser. The main advantage of a phonon laser is that, since sound waves propagate at a much slower speed than light waves, they have a shorter wavelength at the same frequency, which allows for highly precise nondestructive measurements and imaging to be performed.

1.3.2 Mechanism of laser

To implement a laser, the initial requirement for laser activity is the process of stimulated emission (see Figure 1.7). Stimulated emission occurs when an excited atom or ion in-

doi:10.6342/NTU202301896

teracts with a photon of electromagnetic radiation, producing an electronic transition that results in the emission of another photon of identical frequency, polarization, phase, and direction. The second crucial requirement for laser activity is the achievement of population inversion, which can be accomplished through the process of optical pumping. Optical pumping involves exciting ground state atoms to higher energy levels through the absorption of pump light. As these excited electrons decay to a metastable level, nonradiative transitions occur, leading to the establishment of an upper laser level. This population inversion, along with the process of stimulated emission, is what enables the laser to produce a coherent, monochromatic beam of light [37].

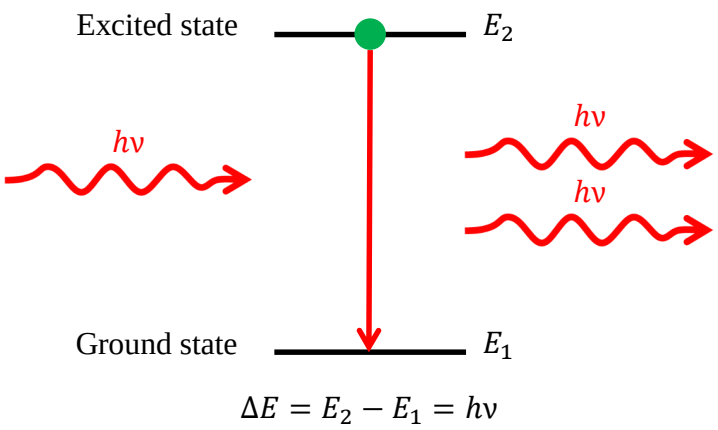

Figure 1.7: The process of stimulated emission occurs when a photon of energy $h\nu$ stimulates the atom to emit a clone photon as it undergoes a downward transition.

Despite similarities to ordinary lasers, Raman lasers operate differently by utilizing stimulated Raman scattering [38] rather than conventional laser principles. Unlike traditional lasers, Raman lasers are not reliant on population inversion for efficient functioning [39, 40, 41]. This process is illustrated in Fig. 1.8, which depicts the stimulated Raman scattering required to achieve a specific phonon state through the mixture of two beams with pumping frequency ω_p and optical Stokes frequency ω_s. The difference between these frequencies must equal the motional frequency ω_{osc}. If the damping of the phonon field is significantly greater than that of the optical Stokes field, Raman lasers can be generated.

Interestingly, the first phonon laser was designed to operate without the need for

doi:10.6342/NTU202301896

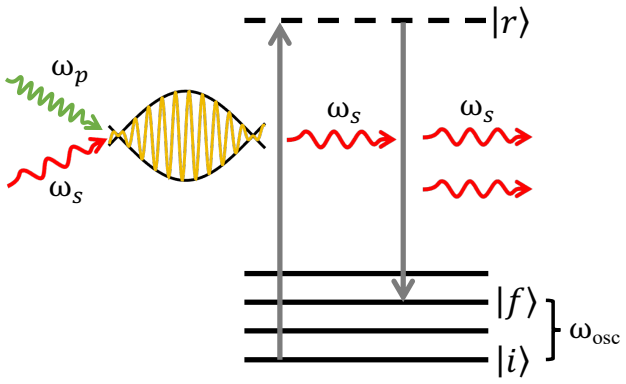

Figure 1.8: The process of stimulated Raman scattering.

population inversion, and as such, shares some similarities with Raman lasers. In other words, the generation of coherent vibrations in a phonon laser is achieved through a self-organizing synchronization process that does not involve population inversion, similar to the case of Raman lasers. In fact, a direct analogy to stimulated Raman scattering can be drawn by allowing the polarization between $|e\rangle$ and $|g\rangle$, i.e. σ^+, in Fig. 1.9 to be treated as the Stokes wave [11]. But the condition in phonon lasers should be that the damping of the optical Stokes field is significantly greater than that of the phonon field [42].

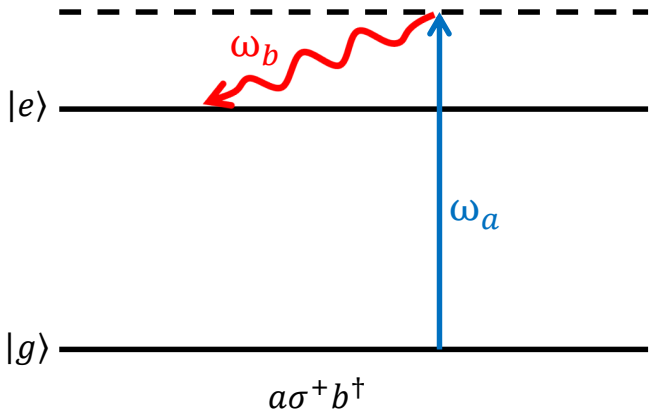

Figure 1.9: The production of the phonon through stimulated Raman scattering, where a is an annihilation operator of the pump light with a frequency ω_a and $b^\dagger$ is a creation operator of a phonon with a frequency ω_b.

Subsequently, researchers have developed phonon lasers by utilizing various preexisting optical laser technologies, including the three-level laser [19], the quantum cascade laser [18, 26], and the Brillouin laser [17, 20, 21, 22, 24, 25].

doi:10.6342/NTU202301896

1.3.3 Properties of laser

Both phonon lasers and optical lasers are characterized by their exceptional properties of monochromaticity, coherence, and directionality. In this section, we will discuss these properties in the context of both phonon lasers and optical lasers.

1.3.3.1 Monochromaticity

The bandwidth of white light spans the entire visible spectrum, which is approximately 400 THz. When white light passes through a dispersive glass prism, it is separated into its component wavelengths and dispersed into the colors of the visible spectrum (Fig. 1.10(a)). Even light that appears red to the naked eye, such as white light filtered through a red filter, is also separated by the prism into its constituent wavelengths. While the bandwidth of the filtered light is narrower than that of white light, the prism still produces a range of colors, from deep red to light red, as shown in Fig. 1.10(b). In contrast, the light from a red laser is unaffected by the prism (Fig. 1.10(c)), because the linewidth of the laser is extremely small compared to that of filtered light. The monochromaticity of a laser is due to stimulated emission, although a laser cannot be perfectly monochromatic and must have some non-zero linewidth. This is because a perfectly monochromatic wave would violate the uncertainty principle, which is a fundamental principle of quantum physics.

The concept of monochromaticity also applies to the phonon laser system. At a given temperature, an object undergoes random motion in accordance with Bose-Einstein statistics. When subjected to external forces, the object may exhibit self-sustained oscillations above a certain threshold, gaining energy from the sources. The object oscillates at a specific frequency, albeit with some degree of uncertainty.

1.3.3.2 Coherence

A laser exhibits both spatial and temporal coherence (see Figure 1.11(a)), which are essential characteristics that make laser light so unique and valuable in various applications. Spatial coherence refers to the uniformity of the phase of the electromagnetic wave in the transverse direction (perpendicular to the beam propagation direction) (see Fig-

doi:10.6342/NTU202301896

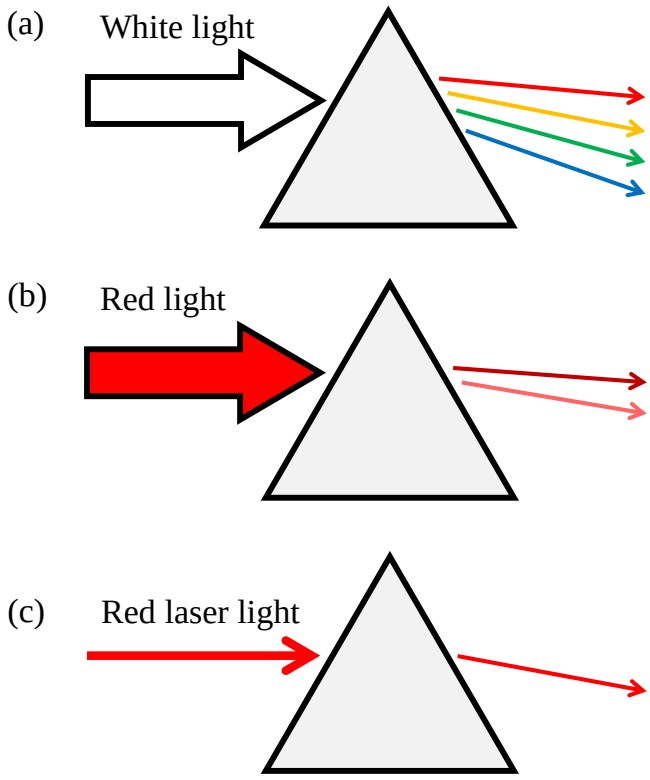

Figure 1.10: The schematic dispersion of (a) white light, (b) red filtered light, and (c) red laser light.

ure 1.11(b)). In other words, all points on a plane perpendicular to the beam axis oscillate in phase with each other, creating a well-defined beam profile. This is in contrast to, for example, the light emitted from a light bulb, which has an irregular and random phase distribution in space.

Temporal coherence, on the other hand, refers to the stability and regularity of the oscillation frequency over time. The laser emits light with a narrow linewidth, meaning the oscillation frequency is well defined and remains stable over a long period of time (see Figure 1.11(c)). This is in contrast to, for example, the light emitted from a fluorescent lamp, which has a broad linewidth and a fluctuating frequency over time.

1.3.3.3 Mode competition

Most laser cavities have the ability to oscillate in multiple modes, encompassing various axial and transverse cavity modes. In ring-laser cavities, the oscillation can occur in different directions, and in cavities without Brewster windows, the polarization sense can

doi:10.6342/NTU202301896

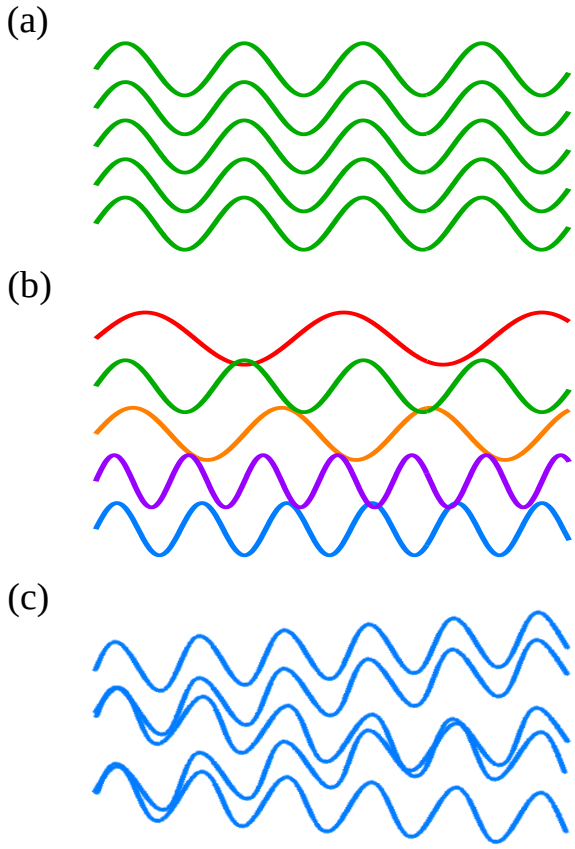

Figure 1.11: (a) Laser waves are both spatially and temporally coherent. (b) Waves are spatially coherent but temporally incoherent. (c) Waves are monochromatic. Spatially, they are incoherent.

also vary. Each mode possesses unique characteristics such as gains, losses, and saturation parameters, and they compete for the population inversion available within the laser. The oscillation of one mode can diminish the gain available for other modes and, in certain cases, completely suppress them. In 1964, Willis Lamb discovered that the oscillation of one mode can hinder the gain of other modes [43].

The competition among modes within a laser cavity presents a complex problem that necessitates careful consideration of various factors. It is important to account for self-saturation and cross-saturation effects between modes, both in the gain medium and any saturable absorbing media present. Additionally, scattering effects or intracavity modulators can give rise to possible injection locking and frequency pulling effects between modes. The spatial overlap between modes plays a crucial role, where different transverse or axial modes exhibit partial overlapping and spatial separation, leading to regions

doi:10.6342/NTU202301896

of shared and separate population inversion. Furthermore, the spectral overlap between modes must be taken into account, including whether the competing modes have the same or different frequencies, and whether the atomic line is homogeneous or inhomogeneous. A comprehensive understanding of mode competition in a laser cavity requires a thorough examination of these factors.

In 2014, researchers showcased the mode competition of phonon lasers, a system founded on a highly reflective membrane that sustains numerous mechanical modes and radiation pressure coupling. Their findings indicated that despite the mechanical gain surpassing losses for multiple modes, the steady-state condition consistently yields a solitary oscillating mode [20].

1.4 Electromagnetically-induced-transparency (EIT) cooling

1.4.1 Cooling in Lamb-Dicke regime

In order to determine the cooling and heating rates of a trapped ion driven by a laser with a scattering rate $W(\Delta)$ and laser detuning Δ, we need to consider the absorption-emission cycle that occurs as the ion transitions between states $|g,n_1\rangle$, $|e,n_2\rangle$, and $|g,n_3\rangle$ [44, 45]. One approach would involve calculating the scattering rates for all possible combinations of vibrational states (n_1,n_2,n_3) and deriving a set of rate equations to describe the probability $P(n)$ of the ion occupying a specific motional state n. However, for simplicity, we will assume that the ion has undergone precooling, such as Doppler cooling, which results in a thermal distribution of vibrational states that falls within or is close to the Lamb-Dicke regime, characterized by $\eta^2\bar{n} \leq 1$ (η represents the Lamb-Dicke parameter and $\bar{n}$ is the mean occupation of the thermal motional state). Although this approximation does not capture the complete dynamics of cooling, it provides useful expressions for the cooling limit and rate towards the final state, assuming the cooling method reaches the Lamb-Dicke regime. We also assume that we have knowledge of the scattering rate $W(\Delta)$

doi:10.6342/NTU202301896

for an atom at rest, which can be obtained by solving the Bloch equations for the atom and calculating the steady-state population ρ_{ee} in the excited state. The relationship between the scattering rate $W(\Delta)$ and the population ρ_{ee} is given by $W(\Delta) = \gamma\rho_{ee}$, where γ represents the total decay rate. In the Lamb-Dicke regime, the primary absorption and emission processes are associated with the carrier and first-order red (blue) sidebands, with transition probabilities proportional to Ω^2 and $\eta^2\Omega^2 n(\eta^2\Omega^2(n+1))$ respectively, where Ω is the Rabi frequency. Higher-order processes involving η can be neglected. The scattering of the carrier transition dominates when the motional states remain unchanged, while the red and blue sidebands are responsible for changing the motional states. The possible motional state-changing events are illustrated in Figure 1.12. As a result, the rates for these processes can be expressed as follows:

$$R_{n\to n+1} = W(\Delta)\,\eta^2(n+1) + W(\Delta-\nu)\,\eta^2(n+1), \tag{1.4.1}$$

$$R_{n\to n-1} = W(\Delta)\,\eta^2 n + W(\Delta+\nu)\,\eta^2 n, \tag{1.4.2}$$

where ν represents the motional frequency.

Furthermore, the rate equation can be written as

$$\begin{aligned}\dot{P}_n &= R_{n+1\to n}P_{n+1} - R_{n\to n-1}P_n + R_{n-1\to n}P_{n-1} - R_{n\to n+1}P_n \\ &= A_-\left[(n+1)P_{n+1} - nP_n\right] + A_+\left[nP_{n-1} - (n+1)P_n\right],\end{aligned} \tag{1.4.3}$$

with the n-independent coefficients

$$A_\pm = \eta^2\left[W(\Delta) + W(\Delta\mp\nu)\right]. \tag{1.4.4}$$

To obtain the equation of the average thermal occupation number, the rate equation can be converted into the following equation

$$\dot{\overline{n}} = \sum_{n=1}^{\infty} n\dot{P}_n = -(A_- - A_+)\,\overline{n} + A_+. \tag{1.4.5}$$

doi:10.6342/NTU202301896

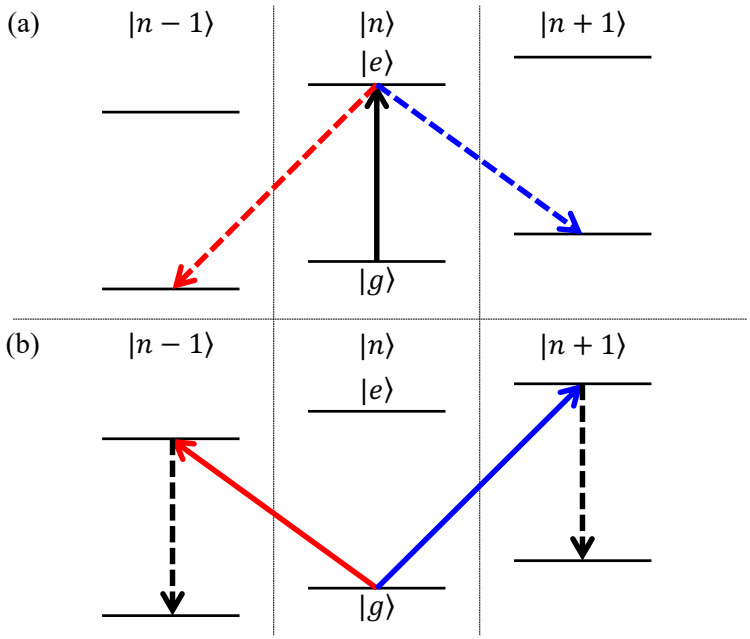

Figure 1.12: The dominant motional-state-changing events: (a) The laser beam is absorbed by the carrier transition thereafter spontaneously emit to the red and blue sideband. (b) The laser beam is absorbed by the red and blue sideband transition thereafter spontaneously emit to the carrier transition. .

If the cooling rate, represented by the expression $-(A_- - A_+)$, remains lower than zero, then the value of $\overline{n}$ will gradually move towards the final cooling state, the steady state of Eq. 1.4.5 given by

$$\overline{n}_s = \frac{A_+}{A_- - A_+} = \frac{W(\Delta) + W(\Delta - \nu)}{W(\Delta + \nu) - W(\Delta - \nu)}. \tag{1.4.6}$$

To achieve optimal cooling performance with a general scattering rate, it is desirable to minimize the final average thermal occupation number, $\overline{n}_s$. This can be achieved by ensuring that the scattering rate on the red sideband, $W(\Delta + \nu)$, is significantly higher than the scattering rates on the carrier and blue sidebands, $W(\Delta)$ and $W(\Delta - \nu)$, respectively.

1.4.2 Scattering rates in EIT cooling

The main concept behind EIT cooling in a Λ system is to utilize a dark resonance to effectively eliminate the carrier scattering [46]. By carefully selecting the parameters of the two light fields that drive the system, we can achieve a situation where the scattering

doi:10.6342/NTU202301896

rate on the red sideband greatly exceeds the scattering rate on the blue sideband, resulting in optimal cooling outcomes.

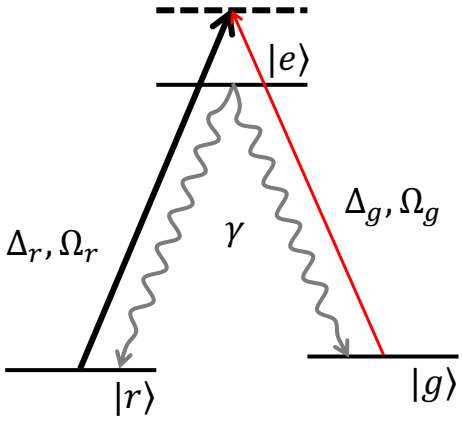

Figure 1.13: Levels, detunings, Rabi frequencies, and decay rates used to calculate electromagnetically induced transparency (EIT).

The Λ-type EIT system is comprised of three states: a ground state $|g\rangle$, a metastable state $|r\rangle$, and an excited state $|e\rangle$, as depicted in Figure 1.13. The excited state has a linewidth of γ and is coupled to states $|g\rangle$ and $|r\rangle$ via the dipole transition. The transition $|r\rangle \rightarrow |e\rangle$ is excited by a coupling laser with a detuning of $\Delta_r = \omega_r - \omega_{er}$ and a Rabi frequency of Ω_r, where ω_r is the laser frequency and ω_{er} is the frequency of the bare atomic transition $|r\rangle \rightarrow |e\rangle$. The absorption spectrum of this system can be observed by exciting the transition $|g\rangle \rightarrow |e\rangle$ with a cooling laser at frequency $\omega_{eg} + \Delta_g$ and Rabi frequency Ω_g. Therefore, the Bloch equations of the system are

$$
\begin{aligned}
\dot{\rho}_{rr} &= i\frac{\Omega_r}{2}\left(\rho_{re} - \rho_{er}\right) + \gamma_r \rho_{ee}, \\
\dot{\rho}_{gg} &= i\frac{\Omega_g}{2}\left(\rho_{ge} - \rho_{eg}\right) + \gamma_g \rho_{ee}, \\
\dot{\rho}_{rg} &= i\left[\left(\Delta_g - \Delta_r\right)\rho_{rg} + \frac{\Omega_g}{2}\rho_{re} - \frac{\Omega_r}{2}\rho_{eg}\right], \\
\dot{\rho}_{re} &= i\left[\frac{\Omega_r}{2}\left(\rho_{rr} - \rho_{ee}\right) + \frac{\Omega_g}{2}\rho_{rg} - \Delta_r \rho_{re}\right] - \frac{\gamma}{2}\rho_{re}, \\
\dot{\rho}_{ge} &= i\left[\frac{\Omega_g}{2}\left(\rho_{gg} - \rho_{ee}\right) + \frac{\Omega_r}{2}\rho_{gr} - \Delta_g \rho_{ge}\right] - \frac{\gamma}{2}\rho_{ge},
\end{aligned}
\tag{1.4.7}
$$

with $\gamma = \gamma_g + \gamma_r$. Using the conservation of probability $\rho_{gg} + \rho_{rr} + \rho_{ee} = 1$, one can obtain

doi:10.6342/NTU202301896

th steady solution for ρ_{ee}:

$$\rho_{ee}(\Delta) = \frac{4\Delta^2\Omega_g^2\Omega_r^2\gamma}{D} \tag{1.4.8}$$

,where $\Delta = \Delta_g - \Delta_r$ and

$$\begin{aligned} D = {} & 8\Delta^2\Omega_r^2\Omega_g^2\gamma + 4\Delta^2\gamma^2\left(\Omega_r^2\gamma_g + \Omega_g^2\gamma_r\right) + 16\Delta^2\left(\Delta_r^2\Omega_g^2\gamma_r + \Delta_g^2\Omega_r^2\gamma_g\right) \\ & + 8\Delta_r\Delta\Omega_g^4\gamma_r - 8\Delta_g\Omega_r^4\gamma_g + \left(\Omega_r^2 + \Omega_g^2\right)\left(\Omega_r^2\gamma_g + \Omega_g^2\gamma_r\right). \end{aligned}$$

By assuming $\Delta_r \simeq \Delta_g$ and $\Omega_g \ll (\Omega_r, \Delta_r)$ and setting $\gamma_g = \alpha\gamma$, the scattering rate in EIT system yields

$$W(\Delta) = \gamma\rho_{ee}(\Delta) \simeq \frac{\Delta^2\Omega_g^2\gamma}{\alpha\left[\Delta^2\gamma^2 + 4\left(\frac{\Omega_r^2}{4} - \Delta\Delta_g\right)^2\right]}. \tag{1.4.9}$$

The qualitative behavior of the scattering rate versus detuning Δ_g is depicted in Figure 1.14. It can be observed that the scattering rate of the carrier transition is completely suppressed at $\Delta = 0$. Moreover, the maximum position is given by

$$\Delta_\pm = \frac{1}{2}\left(\pm\sqrt{\Delta_r^2 + \Omega_r^2} - \Delta_r\right). \tag{1.4.10}$$

To maximize the scattering rate of the red-sideband, it is necessary to align the narrow bright resonance at positive detuning with the red sideband, i.e., $\Delta_+ = \nu$. Consequently, the cooling limit for the EIT cooling is

$$\overline{n}_s = \frac{W(\Delta - \nu)}{W(\Delta + \nu) - W(\Delta - \nu)} = \left(\frac{\gamma}{4\Delta_r}\right)^2. \tag{1.4.11}$$

To ensure $\overline{n}_s \ll 1$, the detuning has to be choosed much larger than the spontaneous decay rate γ.

doi:10.6342/NTU202301896

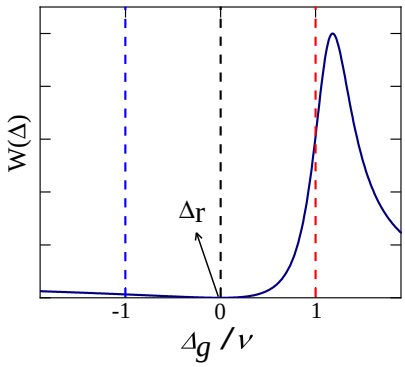

Figure 1.14: On the $|g\rangle \rightarrow |e\rangle$ transition, the scattering rate is qualitatively affected as Δ_g for $\Delta_r > 0$.

1.5 Open quantum system

When describing a quantum system, we typically begin by defining its Hamiltonian and deriving its corresponding equations of motion. However, it is often impractical to describe the system in terms of the Hamiltonian of the entire universe due to the immense size of the associated Hilbert space and the abundance of extraneous information. Therefore, it becomes necessary to identify and isolate the relevant environment that primarily affects the system, and to study its underlying physics.

In the subsequent section, we will demonstrate the standard approach to addressing open quantum systems. We will discuss various techniques and methods that allow us to effectively and accurately analyze the dynamics of the system-environment interaction, and to extract meaningful information about the system itself.

1.5.1 Preliminary

Generally, the system affected by its reservoir can be described by the Hamiltonian

$$H = H_S + H_R + V, \tag{1.5.1}$$

doi:10.6342/NTU202301896

where H_S, H_R, and V are the Hamiltonian of the system, the reservoir, and the interaction between them, respectively. The corresponding equation is given by

$$i\hbar\frac{d\rho}{dt} = [H, \rho], \tag{1.5.2}$$

where ρ is the total density operator. To clarify how the reservoir affect the system, we turn the Schrodinger picture to the interaction one:

$$i\hbar\frac{d\tilde{\rho}}{dt} = \left[\tilde{V}, \tilde{\rho}\right], \tag{1.5.3}$$

where

$$\tilde{\rho} = e^{\frac{i}{\hbar}(H_S+H_R)t}\rho e^{\frac{-i}{\hbar}(H_S+H_R)t} \tag{1.5.4}$$

and

$$\tilde{V} = e^{\frac{i}{\hbar}(H_S+H_R)t}V e^{\frac{-i}{\hbar}(H_S+H_R)t}. \tag{1.5.5}$$

Next, we formally integrate Eq. (1.5.3)

$$\tilde{\rho}(t) = \rho(0) + \frac{1}{i\hbar}\int_0^t d\tau \left[\tilde{V}(\tau), \tilde{\rho}(\tau)\right] \tag{1.5.6}$$

and substituting back in Eq. (1.5.3), we get

$$\frac{d\tilde{\rho}}{dt} = \frac{1}{i\hbar}\left[\tilde{V}(t), \rho(0)\right] - \frac{1}{\hbar^2}\int_0^t d\tau \left[\tilde{V}(t), \left[\tilde{V}(\tau), \tilde{\rho}(\tau)\right]\right]. \tag{1.5.7}$$

Tracing out the reservoir's degrees of freedom results in the quantum master equation of the system:

$$\frac{d\tilde{\rho}_S}{dt} = \frac{1}{i\hbar}Tr_R(\left[\tilde{V}(t), \rho(0)\right]) - \frac{1}{\hbar^2}\int_0^t d\tau Tr_R(\left[\tilde{V}(t), \left[\tilde{V}(\tau), \tilde{\rho}(\tau)\right]\right]). \tag{1.5.8}$$

The density operator for the system is $\tilde{\rho}_S = Tr_R(\tilde{\rho})$, and the Eq. (1.5.8) is exact and

doi:10.6342/NTU202301896

hard to solve.

1.5.2 Born-Markov approximation

To make Eq. (1.5.8) easily solve, we assume that the system and the reservoir do not interact at the beginning, which implies they are factorized initially:

$$\rho(0) = \rho_S(0) \otimes \rho_R(0). \tag{1.5.9}$$

If the coupling is weak enough and also the dimension of the reservoir is very large, the total density operator ρ at all times can be written as

$$\rho(t) \approx \rho_S(t) \otimes \rho_R(0) + O(V). \tag{1.5.10}$$

The weak-coupling assumption is also known as Born approximation. Ignoring terms higher than second order in V and assuming $Tr_R(\left[\tilde{V}(t), \rho(0)\right]) = 0$, we write Eq. (1.5.8) as

$$\frac{d\tilde{\rho}_S}{dt} = -\frac{1}{\hbar^2}\int_0^t d\tau Tr_R(\left[\tilde{V}(t), \left[\tilde{V}(\tau), \tilde{\rho}_S(\tau) \otimes \rho_R(0)\right]\right]). \tag{1.5.11}$$

Eq. (1.5.11) is still complicated because of the memory effect, That is, the future evolution of $\tilde{\rho}_S$ is dependent on its past history through the integration over $\tilde{\rho}_S(\tau)$. Such a memory effect is caused by interactions between the system and its reservoir. A system altering the quantum state of the reservoir imposes its current information on the quantum state of the reservoir, which influences the system's future time. Fortunately, the dimension of the reservoir is very large and also the coupling is weak, therefore the reservoir stays its thermal equilibrium state. Hence, the future evolution of $\tilde{\rho}_S$ now depends on its present time ($\tilde{\rho}_S(\tau)$ is replaced by $\tilde{\rho}_S(t)$). This approximation is also known as Markov approximation. The quantum master equation under Born-Markov approximation is writ-

doi:10.6342/NTU202301896

ten as

$$\frac{d\tilde{\rho}_S}{dt} = -\frac{1}{\hbar^2}\int_0^\infty d\tau Tr_R([\tilde{V}(t),[\tilde{V}(\tau),\tilde{\rho}_S(t)\otimes\rho_R(0)]]). \tag{1.5.12}$$

1.5.3 Master equation of a damped harmonic oscillator

In this section, we consider a typical case - a damped harmonic oscillator [47]. The Hamiltonian is expressed as

$$\begin{aligned} H_S &= \hbar\omega_0 a^\dagger a, \\ H_R &= \hbar\sum_i \omega_i b_i^\dagger b_i, \\ V &= \hbar\sum_i g(\omega_i)(a^\dagger b_i + a b_i^\dagger), \end{aligned} \tag{1.5.13}$$

with $a^\dagger(a)$ and $b_i^\dagger(b_i)$ signifying the creation (annihilation) operator of the system and the reservoir, respectively. The coupling between the system, characterized by its frequency ω_0, and the reservoir, identified by its mode index i and frequency ω_i, is denoted as $g(\omega_i)$. To simplify the analysis, we have employed the rotating-wave approximation (RWA) argument, which involves neglecting the rapidly oscillating terms. As a result, we retain only the counter-rotating terms, which allow us to study the non-classical features of the system. This approach reduces the complexity of the analysis and provides a more tractable mathematical framework for investigating the dynamics of the system.

The interaction Hamiltonian for this model is

$$\tilde{V} = \hbar\sum_i g(\omega_i)(a^\dagger b_i \exp[i(\omega_0-\omega_i)t] + b_i^\dagger a \exp[-i(\omega_0-\omega_i)t]). \tag{1.5.14}$$

By performing the substitution of Eq. (1.5.14) into Eq. (1.5.12), we can derive the

doi:10.6342/NTU202301896

expression

$$\frac{d\tilde{\rho}_S}{dt} = -i\Delta\omega[a^\dagger a, \tilde{\rho}_S] + \pi g(\omega_0)^2 D(\omega_0)(1+\langle n(\omega_0)\rangle)([a, \tilde{\rho}_S a^\dagger] + [a\tilde{\rho}_S, a^\dagger]) + \pi g(\omega_0)^2 D(\omega_0)\langle n(\omega_0)\rangle([a^\dagger, \tilde{\rho}_S a] + [a^\dagger \tilde{\rho}_S, a]). \quad (1.5.15)$$

To obtain Eq. (1.5.15), we relied on the use of certain properties, namely

$$Tr_R(b_i^\dagger b_j \rho_R(0)) = \delta_{ij}\langle n(\omega_i)\rangle, \quad (1.5.16)$$

$$Tr_R(b_i b_j \rho_R(0)) = 0, \quad (1.5.17)$$

$$\Delta\omega = P\int_0^\infty d\omega_i \frac{g(\omega_i)^2 D(\omega_i)}{\omega_0 - \omega_i}, \quad (1.5.18)$$

for the density function $D(\omega)$, and

$$\int_0^\infty d\tau \exp[\pm i(\omega_0 - \omega_i)\tau] = \pi\delta(\omega_0 - \omega_i) \pm P(\frac{1}{\omega_0 - \omega_i}). \quad (1.5.19)$$

The commonly adopted formulation of the master equation takes the form

$$\frac{d\tilde{\rho}_S}{dt} = -i\Delta\omega[a^\dagger a, \tilde{\rho}_S] - \frac{\kappa}{2}(1+\langle n(\omega_0)\rangle)(\tilde{\rho}_S a^\dagger a + a^\dagger a\tilde{\rho}_S - 2a\tilde{\rho}_S a^\dagger) - \frac{\kappa}{2}\langle n(\omega_0)\rangle(\tilde{\rho}_S aa^\dagger + aa^\dagger\tilde{\rho}_S - 2a^\dagger\tilde{\rho}_S a), \quad (1.5.20)$$

where $\kappa = 2\pi g(\omega_0)^2 D(\omega_0)$.

In order to gain a comprehensive understanding of the population distribution, we utilize the probability rate equation, which is obtained by recasting the master equation and corresponds to its diagonal term, denoted as

$$\frac{dP_n}{dt} = -\kappa(1+\langle n(\omega_0)\rangle)(nP_n - (n+1)P_{n+1}) - \kappa\langle n(\omega_0)\rangle((n+1)P_n - nP_{n-1}). \quad (1.5.21)$$

doi:10.6342/NTU202301896

1.6 Dissertation outline

The dissertation is structured as follows. Chapter 2 provides a comprehensive literature review, where we meticulously examine the research contributions of various groups. Subsequently, we introduce a novel phonon cavity model that we propose. This model is carefully formulated, considering crucial aspects such as cavity decay rate computations and an in-depth analysis of its behavior under varying numbers of optical tweezers. Additionally, we investigate the dispersion relation of an ion chain within the context of this phonon cavity model, thereby deriving the propagating speed of phonons.

Moving on to Chapter 3, we expound on the application of the phonon cavity in the realization of a phonon laser. We offer a thorough discussion of the laser's behavior, encompassing its unique properties and underlying mechanisms.

Chapter 4 centers on the implementation of multiple EIT cooling techniques on the phonon cavity. Our investigation focuses on exploring the cooling limits and cooling rates achievable through this approach.

Lastly, in Chapter 5, we present our comprehensive conclusions derived from the entire research endeavor. Moreover, we provide an outlook on potential future directions and research avenues that could arise from this pioneering work.

doi:10.6342/NTU202301896

doi:10.6342/NTU202301896

Chapter 2

Trapped ion arrays with optical tweezers

2.1 Advantages of the setup

Ion systems possess several advantages over alternative platforms, including enduring atomic coherence, indistinguishable qubits, a dependable Coulomb interaction facilitated by lasers, and the ability to engineer deterministic control over entanglement. However, the primary obstacle for ion systems lies in achieving scalability.

Numerous scalable strategies have been proposed to address the challenge of scalability. These approaches encompass ion shuttling [48, 49, 50, 4], quantum networks [4, 51, 52], and arrays of microtraps [53, 54]. Nevertheless, these proposals introduce fresh challenges associated with hardware fabrication (shuttling, microtraps), precise control of movement (shuttling), sluggish processing speed (shuttling), and probabilistic and lossy quantum interfacing (quantum network).

Achieving scalability poses significant challenges when scaling up the 1D geometry of a Paul trapped ion array. The following are key obstacles that impede scalability:

1. Architecture Challenge: Expanding the ion array requires constructing a larger trap. The architecture should allow for individual qubit addressing and scalability. To avoid cross-talk between neighboring ions, the spacing between ions (d_0) must be

doi:10.6342/NTU202301896

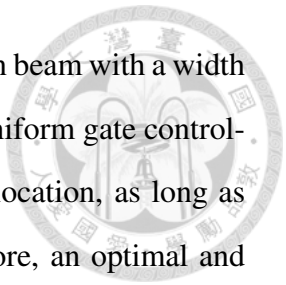

maintained at a few microns to accommodate a focused Gaussian beam with a width approximately half of the spacing. It is advantageous to have uniform gate controlling parameters throughout the crystal, regardless of the gate location, as long as the gate distance between target qubits remains fixed. Therefore, an optimal and uniform geometry is desired [55]. Anharmonic ion trap potentials have been successfully implemented by several research groups to address this challenge [56, 57].

2. Array Stability and Cooling Challenge: In very large linear ion arrays, maintaining a flat bottom trap ensures even distribution of ions. However, this causes the disappearance of low-frequency modes associated with longitudinal motion. For instance, the ground mode corresponds to collective macroscopic translation, which can cause qubit ions to deviate from their designated positions and become difficult to address. Moreover, these motional states are susceptible to rapid heating due to divergent phonon numbers, posing a stability threat to the array structure.

3. Gate Design Challenge: Achieving a two-qubit gate in the adiabatic regime becomes problematic in a large array due to the indistinguishable collective motional spectrum. However, gate operations can still be performed by considering the influence of multi-modes on the local motional degrees of freedom of the involved ions. This suggests the use of fast gate operations to prevent the spread of local motion throughout the entire system. Two major protocols for fast gates are the push gate scheme, based on pulsed lasers [51, 58, 59, 60], and the pulse shaping scheme, based on continuous-wave lasers [32, 55, 61, 62, 63]. These fast gates have demonstrated high fidelity but require high-intensity laser power.

Our research group has addressed the architecture and cooling challenges by proposing a scalable trapping scheme for a large linear ion crystal. This scheme incorporates the use of optical tweezers to enhance stability and control within the system (refer to Figure 2.1) [1]. The core concept involves utilizing optical tweezers to immobilize specific ions, inducing modifications in the motional spectrum. This manipulation preserves the lowest motional frequency, preventing position fluctuations and phonon number divergence.

doi:10.6342/NTU202301896

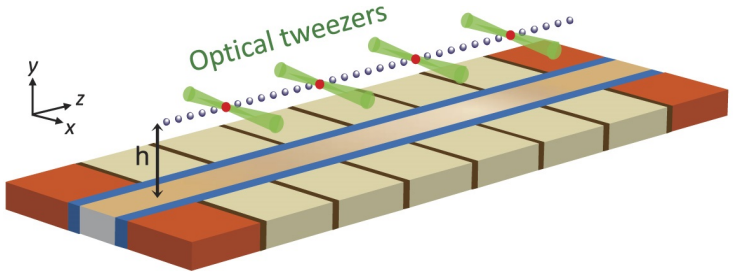

Figure 2.1: A scalable optical tweezers-based ion trap architecture for a planar quantum computing system. (retrieved from Ref.[1])

2.2 Applications of optical tweezers in trapped ion systems

The proposed setup incorporating optical tweezers has been adopted in several articles for quantum computing, quantum simulation, and quantum information processing (QIP) purposes. Here is a summary of the specific tasks addressed in each article:

1. In the study by Olsacher *et al.* [64], scalable and parallel entangling gates in trapped-ion systems are implemented using engineered localized phonon modes. The authors demonstrate the customization of these modes through programmable optical tweezers, enabling simultaneous entangling gate operations on subsets of qubits.

2. Espinoza *et al.* [65] introduce a method for generating programmable interactions in trapped-ion quantum simulators, applicable to both one- and two-dimensional setups. Optical tweezers are utilized to engineer the sound-wave spectrum of trapped ion crystals, surpassing the limitations of current experimental setups. This enables tunable interactions and connectivity among ion qubits.

3. Teoh *et al.* [66] outline protocols for programming an optical tweezers array to achieve precise control over target phonon modes. They explore applications in simulating quantum thermodynamics, enhancing sympathetic cooling, and implementing quantum logic gates in multispecies ion systems. The authors discuss the necessary optical parameters and potential effects in QIP.

doi:10.6342/NTU202301896

4. Bond *et al*. [67] investigate the resilience of their findings in the presence of experimental imperfections such as micromotion, local stress, and intensity noise. They show that micromotion effects can be mitigated through optimized tweezer patterns and that additional flexibility gained from local stress is negligible. The authors conclude that optical tweezers remain valuable for controlling interactions in trapped-ion quantum simulators, even with imperfections.

5. Mazzanti *et al*. [68] propose a scalable architecture for trapped-ion quantum computing, combining optical tweezers with oscillating electric fields. This approach enables long-range qubit-qubit interactions without relying on ground-state cooling or the Lamb-Dicke approximation. The authors examine the effects of imperfect cooling and unwanted qubit-motion entanglement and discuss the feasibility of implementing state-dependent tweezers in the laboratory.

6. In a recent study by Mazzanti *et al*. [69] quantum logic gates are practically implemented in trapped-ion systems using tightly focused optical tweezers. The authors demonstrate qubit-state dependent forces resulting from localized intensity variations near the tweezers' focal point, enabling gate operations between pairs of ion qubits. The proposed design eliminates the need for ground-state cooling and counter-propagating laser fields. The study investigates the impact of imperfections, particularly pointing errors in the tweezers, on gate fidelity.

Collectively, these articles explore the capabilities of optical tweezers in trapped-ion systems, addressing various aspects such as entangling gates, programmable interactions, quantum thermodynamics, imperfections, and practical gate implementations.

2.3 Quantum simulation with phonons

Researchers in this particular configuration have shown limited attention to the utilization of motional states. However, it is crucial to acknowledge that the Hilbert space associated with motional states is larger than the Hilbert space corresponding to internal states. As

doi:10.6342/NTU202301896

a result, motional states hold significant potential for enabling quantum simulation and quantum computing.

Successful experimental realization of a conditional beam splitter gate using a single trapped ion has been achieved, as demonstrated by existing practical experiments [10]. In this setup, two motional modes undergo the beam splitter transformation based on the spin state of the ion. This configuration effectively emulates a Fredkin gate, which is a fundamental component in quantum computing.

Phonons have proven to be versatile resources not only in quantum computing but also in quantum simulation. Researchers have effectively utilized phonons for performing arithmetic operations [8] and verifying the Jarzynski equality [9], which embodies the second law of thermodynamics. Furthermore, progress has been made in generating a phonon laser [11]. However, it is worth noting that the current techniques for phonon laser generation deviate from the conventional use of an optical cavity, challenging our conventional understanding of an optical laser. Given this, we propose a novel model that aligns with our intuitive comprehension of a conventional optical laser.

2.4 Model

In this section, we propose the implementation of optical tweezers on a $^{40}Ca^{+}$ ion chain to create a phonon cavity and determine the corresponding decay rate. Subsequently, a comprehensive analysis of its physical characteristics is conducted, culminating in the calculation of the phonon velocity through the dispersion relation.

2.4.1 Hamiltonian with optical tweezers

The Hamiltonian of a long ion chain with optical tweezers in the z-direction is given by:

$$H_m = \sum_i \frac{p_i^2}{2m} + \sum_{i,j} A_{ij} z_i z_j,$$

where the elements of A_{ij} are defined as follows:

doi:10.6342/NTU202301896

$$A_{ij} = \begin{cases} m\omega_z^2 + m\omega_{tw,i}^2 + \sum_{l=2}^{N} \sum_{i=1}^{l-1} \frac{e^2}{4\pi\epsilon_0} \frac{2}{|z_i^0 - z_l^0|^3}, & i = j \\ -\frac{e^2}{4\pi\epsilon_0} \frac{2}{\left|z_i^0 - z_j^0\right|^3}. & i \neq j \end{cases}$$

In this expression: m denotes the mass of the ion; ω_z represents the trapping frequency along the z-directions; $\omega_{tw,i}^2$ denotes the frequency provided by the optical tweezers experienced by the ith ion; e signifies the charge of a single ion; ϵ_0 represents the vacuum permittivity; z_i^0 epresents the equilibrium position of the ith ion. It is important to note that we have employed the harmonic approximation for the interaction, assuming that the ion chain is currently in equilibrium.

It is worth mentioning that in the case of a uniformly arranged ion crystal, the frequency scale that represents the momentum exchange between neighboring ions is referred to as ω_0, defined as $\omega_0 \equiv [e^2/(4\pi\epsilon_0 m d_0^3)]^{1/2}$. This particular value is obtained by balancing the energy scales of local oscillation and mutual Coulomb interaction.

In order to establish a phonon cavity within such a system, we can apply optical tweezers to specific ions. Due to the significantly higher frequency of the tweezers compared to the local motional frequency of the ions, the motional spectrum of the overall system is altered, resulting in the formation of distinct vibrational modes. Notably, the internal vibrational mode frequencies are much lower than those of the tweezers. Consequently, a considerable portion of the phonons directly propagate from the internally trapped ions to the other ions that are not subject to the tweezers' influence. This process effectively leads to the creation of a phonon cavity.

We consider N_S ions within the effective cavity, and only focus on N_S longitudinal modes. The remaining components of the array create a bath that exhibits a wider dispersion band in longitudinal modes compared to the transverse modes. The wall thickness, denoted as w, represents the number of tweezered ions, while the combined thicknesses of the left and right walls are represented as $w_L + w_R$. For this study, we explore symmetric cases with equal values for w_L and w_R, without altering the overall conclusion. The

doi:10.6342/NTU202301896

number of bath ions, N_B, is calculated as $N - w_L - w_R - N_S$, where N represents the total number of ions. We make the assumption that N_B is much larger than N_S, allowing us to approximate the discrete bath spectrum as a continuous band and treat it in a Markovian manner.

We can represent the motional Hamiltonian as follows:

$$H_m = \underbrace{\sum_{i\in C} \frac{p_i^2}{2m} + \sum_{i,j\in C} A_{ij} z_i z_j}_{H_m^C} + \underbrace{\sum_{i\in B} \frac{p_i^2}{2m} + \sum_{i,j\in B} A_{ij} z_i z_j}_{H_m^B} + \underbrace{\sum_{i\in C, j\in B} A_{ij} z_i z_j}_{V_m^{CB}}, \tag{2.4.1}$$

The system is divided into two parts: the cavity part (C) and the environment (B). Here, the elements A_{ij} form the coupling matrix $\mathbf{A} = \mathbf{A}_C \oplus \mathbf{A}_B + \mathbf{A}_{CB}$ where $\mathbf{A}_C$ and $\mathbf{A}_B$ are $N_C \times N_C$ and $(N - N_C) \times (N - N_C)$ submatrices, respectively. The symbol $\oplus$ denotes the direct sum, and $\mathbf{A}_{CB}$ is an $N_C \times (N - N_C)$ matrix that represents the interaction between the two subsystems. To find the normal modes of each subsystem, we can diagonalize their respective coupling matrices. For the cavity part, we obtain the normal modes represented by the annihilation and creation operator pair: $(a_q, a_q^\dagger)$, where the mode index q ranges from 1 to N_C. Here, N_C is the number of ions participating in the cavity, including the ions from the subsystem C as well as the two walls ($N_C = N_S + w_R + w_L$). Similarly, for the environment, we have the normal modes $(a_k, a_k^\dagger)$, where the mode index k ranges from 1 to $N - N_C$. Here, N represents the total number of ions in the entire array. It is important to note that the subsystem C includes the tweezered ions to ensure the smoothness of the dispersion relation of the bath and to maintain Markovian behavior.

Indeed, including the additional $w_L + w_R$ modes from the tweezered ions in subsystem C would result in more modes than the supposed N_S ones. However, we can take advantage of the fact that these extra modes, primarily originating from the tweezered ions, exhibit distinct frequencies and correspond to spatial wavevectors that are highly localized on the tweezered sites. This enables us to differentiate them from the other modes

doi:10.6342/NTU202301896

and identify them as the cavity modes with a one-to-one correspondence.

Under the rotating wave approximation, we can rewrite the Hamiltonian (2.4.1) as follows:

$$H_m = \sum_{q=1}^{N_C} \hbar\omega_q a_q^\dagger a_q + \sum_{k=1}^{N-N_C} \hbar\omega_k a_k^\dagger a_k + \sum_{q\in C, k\in B} g_{qk}\left(a_q a_k^\dagger + a_k a_q^\dagger\right), \tag{2.4.2}$$

Here, ω_q and ω_k represent the eigenfrequencies of the cavity and environment modes, respectively. The term g_{qk} corresponds to the coupling matrix between mode q in the cavity part (C) and mode k in the environment (B). More specifically, we have $g_{qk} = \frac{\hbar}{2m}\sum_{ij} U_{C,qi}^T A_{ij} U_{B,jk} / \sqrt{m^2\omega_q\omega_k}$, where U_C and U_B are the transformation matrices that diagonalize the submatrices $\mathbf{A}_C$ and $\mathbf{A}_B$, respectively. The resulting g_{qk} forms an $N_C \times (N - N_C)$ matrix.

The Heisenberg equations of motion for the field operators are given by:

$$\dot{a}_q = -i\omega_q a_q - i\sum_{k\in B} g_{qk} a_k \tag{2.4.3}$$

$$\dot{a}_k = -i\omega_k a_k - i\sum_{q\in C} g_{qk} a_q. \tag{2.4.4}$$

By integrating out the degrees of freedom of the environment (B), we can derive the following equation for mode q in the cavity (C):

$$\dot{a}_q = -i\omega_q a_q - i\sum_{k\in B} g_{qk} a_k(0)\, e^{-i\omega_k t} - \sum_{k\in B} |g_{qk}|^2 a_q \int_0^t dt' e^{-i(\omega_k-\omega_q)(t-t')}. \tag{2.4.5}$$

The first term contributes to noise, while the second term corresponds to the decay process. The decay rate can be characterized by:

doi:10.6342/NTU202301896

$$\kappa_q \approx 2\sum_{k\in B}|g_{qk}|^2 \int_0^\infty dt' e^{-i(\omega_k-\omega_q)t'} \approx 2\pi \bar{g}_{qq}^2 \rho_B(\omega_q), \tag{2.4.6}$$

where $\bar{g}_{qq}^2$ represents the coarse-grained value of $|g_{qk}|^2$ over a small range of frequencies $\omega_k \approx \omega_q$, and $\rho_B(\omega_q)$ denotes the density of states for the bath's degrees of freedom. In order to compute this expression for a finite N, where the cavity and environment modes are discrete and may not overlap, numerical calculations are performed by plugging in the actual parameters. However, when $N \gg N_C$, we find that the results are consistent with the last approximation, where we take the continuum limit and numerically evaluate the density of states $\rho_B(\omega)$ for the bath's degrees of freedom. Furthermore, we obtain $\bar{g}_{qq}^2$ by averaging $|g_{qk}|^2$ over a small range of frequencies $\omega_k \approx \omega_q$. This approximation justifies the validity of the Markov approximation. It is important to note that we focus only on longitudinal modes, where the bath modes constitute a broadband-like spectrum. This approximation breaks down for transverse modes due to their narrow-band spectral structure.

Firstly, we consider a large but finite system with $N \sim O(10^3)$. By increasing the wall thickness and/or intensifying the tweezer strength, we can anticipate an enhanced isolation of the cavity from the rest of the ion crystal. This isolation leads to a decrease in the decay rate of a cavity mode. Such an approach offers a convenient means of setting up the cavity since the maximum achievable tweezer strength using state-of-the-art techniques is typically limited to a few megahertz due to constraints on atom energy configuration and laser power [70].

In addition, we have performed computations of the mode decay rates for a five-ion cavity ($N_S = 5$) and presented the results in Figure 2.2. The decay rate of approximately $\kappa \sim 10^{-3}\omega_0$ indicates that the cavity mode can persist for roughly a thousand momentum exchanges before it diminishes.

To validate our calculation, we performed a numerical analysis of the real-time population profile, considering all motional degrees of the entire array without any approximations. The results are illustrated in Figure 2.3. When the tweezer frequency (ω_{tw}) is not

doi:10.6342/NTU202301896

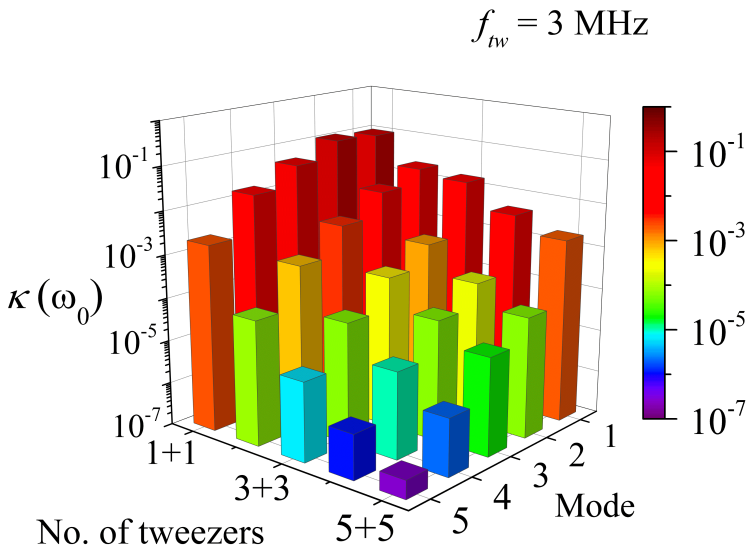

Figure 2.2: The decay rates of the modes were investigated for an $N_S = 5$ cavity with varying wall thickness. The normal modes were ordered based on their frequencies, with mode 1 having the lowest frequency and mode 5 having the highest. The calculations were performed for $^{40}Ca^{+}$ ion crystal with $N > 2000$ ions and an ion separation of 7 μm. The effective cavity near the center of the ion crystal had a tweezer frequency of $f_{tw} = \omega_{tw}/(2\pi) = 3$ MHz. According to their frequencies, the collective normal modes are arranged in the following order (1: lowest; 5: highest).

sufficiently strong compared to ω_0, we observed significant oscillations in the population profile, indicating the presence of non-Markovian behavior. However, as we increased the tweezer frequency to approximately one order of magnitude greater than ω_0, we observed a gradual reduction in non-Markovian effects. In Figure 2.3(d), specifically, where $\omega_{tw}/\omega_0 = 5.9$, the population evolution adhered to the Markovian bath assumption. In this case, we considered an array of over 1000 $^{40}Ca^{+}$ ions, with a chosen distance parameter $d_0 = 7\mu$m and a trap frequency of $\omega_0 = 2\pi \times 0.5$ MHz.

We also find the additivity of the decay rate in the system, which means $\kappa_{w_L+w_R}$ (the decay rate with the thickness $w_L + w_R$) equals to the sum of $\kappa_{w_L+w_L}$ and $\kappa_{w_R+w_R}$ divided by two. As shown in Fig. 2.4, the twice of the decay rate of Fig. 2.4 (b) which tweezers' number is $w_L + w_R = 2+1$ equals to the sum of the decay rate of Fig. 2.4 (a) and (c), which have tweezers' numbers of $w_L + w_R = 1+1$ and $w_L + w_R = 2+2$, respectively.

doi:10.6342/NTU202301896

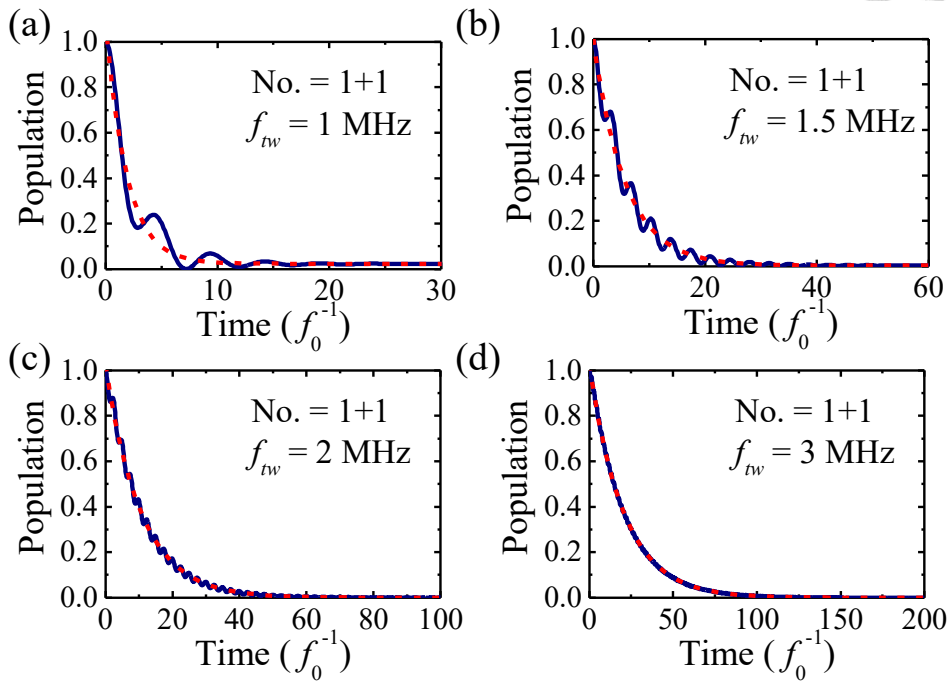

Figure 2.3: We showcase the temporal-population evolution profiles (depicted as blue curves) of a one-ion resonator while systematically varying the frequencies of the tweezers, denoted as $f_{tw} = \omega_{tw}/(2\pi)$. Additionally, we provide exponential fits (illustrated by red dashed lines) characterized by decay rates computed using Eq. (**??**). These calculations were carried out using an ion chain containing more than 1000 $^{40}Ca^{+}$ ions, each separated uniformly by a distance of 7 μm. Throughout our analysis, we employed a frequency unit of $f_0 = \omega_0/(2\pi) = 0.5$ MHz.

2.5 Chapter summary

In this chapter, we review the work of other research groups that have utilized a similar framework. The majority of their efforts focused on employing optical tweezers solely to assist internal degrees of freedom, paying little attention to motional degrees of freedom. Consequently, we propose a novel approach using optical tweezers applied to an ion array to form a phonon cavity.

Next, we compute the cavity decay rate and subsequently analyze how this rate decreases with an increasing number of tweezers. To validate our calculations, we conduct real-time evolutions, revealing that when the tweezers' intensity is insufficient ($\omega_{tw}/\omega_0 < 5.9$), non-Markovian behavior emerges within the system. Additionally, we observe the additivity of the decay rate.

doi:10.6342/NTU202301896

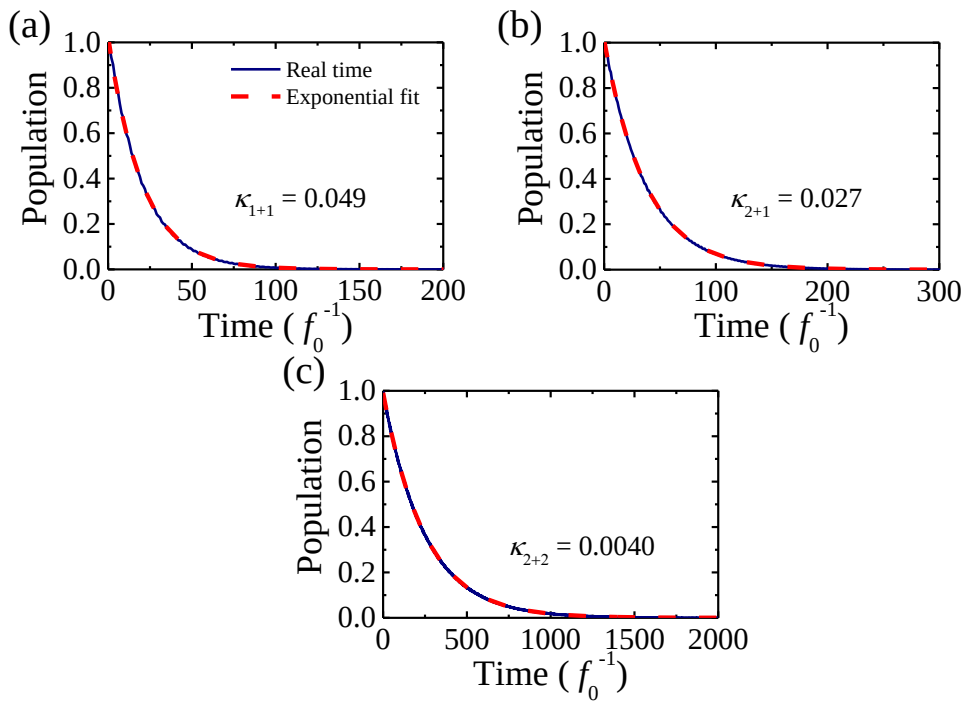

Figure 2.4: The real-time population profiles (represented by blue curves) and the fitted exponential profiles (indicated by red dashed lines) of a single-ion resonator with different tweezers' numbers (a) $w_L + w_R = 1 + 1$ (b) $w_L + w_R = 2 + 1$ and (c) $w_L + w_R = 2 + 2$. The value of the decay rate is fitted by a exponential decay function. The tweezer frequency is $f_{tw} = \omega_{tw}/(2\pi) = 3$ MHz for the effective cavity.

doi:10.6342/NTU202301896

Chapter 3

Phonon laser

The content of this chapter comes from the published paper [71]. In this chapter, we introduce a prototype of a tunable phonon laser that makes use of a large, uniformly arranged ion crystal and optical tweezers. The construction of such a crystal is achievable through the utilization of a long Paul trap [1], microtraps or Penning microtrap arrays [53, 54, 72]. By utilizing optical tweezers on individual ions or on a group of ions in a line, we are able to create a "wall" that effectively impedes the propagation of acoustic waves. Subsequently, our focus shifts to a select group of ions that are trapped within the confinement of two walls, resulting in the creation of an effective phonon cavity. This configuration is illustrated in Figure 3.1. This distinctive characteristic allows us to conceptualize the system as a resonator for a phonon laser.

The proposed scheme offers significant advantages in terms of its simplicity and adaptability for reconfiguration. Notably, optical tweezers can be swiftly activated or deactivated within nanosecond timescales without perturbing the spatial equilibrium of the ion array. Additionally, the size of the effective cavity can be adjusted as needed. The reflectivity of a partial mirror can be controlled by altering the frequencies of the optical tweezers and/or the number of tweezers employed. In the following discussion, we illustrate this concept by investigating the dynamics of lasing while considering that the ion array is exclusively Doppler cooled.

doi:10.6342/NTU202301896

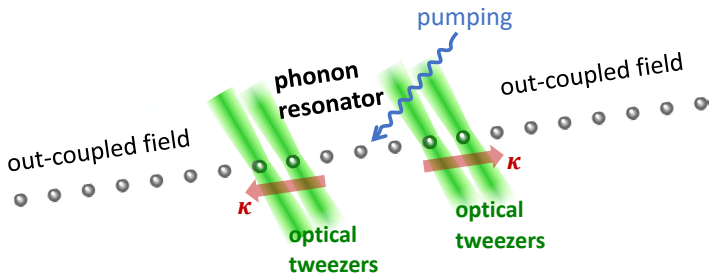

Figure 3.1: A large-scale ion crystal serves as the foundation for an efficient phonon resonator. A partial mirror of the resonator is formed by the tweezered ions.

3.1 Single-mode phonon lasing

3.1.1 Gain and rate equations

In our study, we investigate the phonon lasing mechanism of a resonator consisting of a single ion ($N_S = 1$) that is pumped by blue sideband lasers. The cavity mode frequency typically ranges from hundreds of kilohertz to a few megahertz, and we assume that the sidebands are distinguishable from the carrier transition due to Raman transitions with a few-kilohertz linewidth.

We describe the evolution of the system using a master equation:

$$\dot{\rho} = -\frac{i}{\hbar}[H_S, \rho] - \sum_{\alpha=\pm} \frac{\kappa_{\text{th}}^{\alpha}}{2} \mathcal{L}_a^{\alpha}[\rho] - \frac{\gamma}{2}\mathcal{L}_{\sigma}^{-}[\rho], \tag{3.1.1}$$

Here, ρ represents the density matrix of the system, and it is governed by the system Hamiltonian $H_S/\hbar = -\delta_b\sigma_z/2 + \eta\Omega\left(a^{\dagger}\sigma^{+} + \sigma^{-}a\right)$ in the rotating frame. In this equation, $\sigma^{-} = |g\rangle\langle e|$ and $\sigma^{+} = |e\rangle\langle g|$ are the atomic lowering and raising operators, respectively, between the ground state $|g\rangle$ and the excited state $|e\rangle$, separated by energy $\hbar\omega_{eg}$. Furthermore, $\sigma_z = |e\rangle\langle e| - |g\rangle\langle g|$, γ represents the natural linewidth, $\delta_b = \omega_L - \omega_{eg} - \omega$ is the blue sideband detuning with the driving laser frequency ω_L and the cavity mode frequency ω. The Lamb-Dicke parameter is denoted by η, and Ω represents the Raman Rabi frequency.

The Lindblad superoperators are given by $\mathcal{L}_a^{\pm}[\rho] = a^{\pm}a^{\mp}\rho + \rho a^{\pm}a^{\mp} - 2a^{\mp}\rho a^{\pm}$, where we define $a^{-} = a$ and $a^{+} = a^{\dagger}$ for convenience. Additionally, $\mathcal{L}_{\sigma}^{-}[\rho] = \sigma^{+}\sigma^{-}\rho + \rho\sigma^{+}\sigma^{-} - 2\sigma^{-}\rho\sigma^{+}$. The decay rates are given by $\kappa_{\text{th}}^{+} = n_{\text{th}}\kappa$ and $\kappa_{\text{th}}^{-} = (n_{\text{th}} + 1)\kappa$, where the noise

doi:10.6342/NTU202301896

level n_{th} accounts for the contribution of cavity temperature, which can be estimated by $n_{\text{th}} = [\exp(\frac{\hbar\omega}{k_B T}) - 1]^{-1}$.

It is important to note that the internal state dynamics occur much faster than the motional ones, allowing us to assume that the internal degrees of freedom adiabatically follow the motional operators. To substitute the internal degrees of freedom to the motional operators, we can express the Heisenberg equations of motion for the relevant operators as follows:

$$\dot{a} = -\frac{\kappa}{2}a - i\eta\Omega\sigma^{+} \tag{3.1.2}$$

$$\dot{\sigma}^{+} = \left(-i\delta_b - \frac{\gamma}{2}\right)\sigma^{+} - i\eta\Omega a\sigma_z \tag{3.1.3}$$

$$\dot{\sigma}_z = -\gamma\left(\sigma_z + 1\right) + 2i\eta\Omega\left(\sigma^{-}a - a^{\dagger}\sigma^{+}\right) \tag{3.1.4}$$

By assuming $\dot{\sigma}^{+} \approx 0$, we can immediately obtain

$$\sigma^{+} \approx -\frac{\eta\Omega a\sigma_z}{\delta_b - i\frac{\gamma}{2}}. \tag{3.1.5}$$

Therefore, the equation for $\dot{a}$ becomes:

$$\dot{a} = -\frac{\kappa}{2}a - \frac{1}{2}\frac{\gamma\left|\eta\Omega\right|^2}{\delta_b^2 + \left(\frac{\gamma}{2}\right)^2}\sigma_z a + \text{shift} + \text{noise}. \tag{3.1.6}$$

It's important to note that the noise term must be present to ensure a valid field operator that satisfies $[a, a^{\dagger}] = 1$. However, both the shift and noise terms are irrelevant for the current discussion. The gain, denoted as $\mathcal{G}$, can now be identified as:

$$\mathcal{G} = -\frac{\gamma\left|\eta\Omega\right|^2}{\delta_b^2 + \left(\frac{\gamma}{2}\right)^2}\sigma_z. \tag{3.1.7}$$

By substituting Eq. (3.1.5) into Eq. (3.1.4) and assuming $\dot{\sigma}_z \approx 0$, we have:

doi:10.6342/NTU202301896

$$\begin{aligned}\sigma_z &= -\left(I + \frac{2}{\delta_b^2 + \left(\frac{\gamma}{2}\right)^2}|\eta\Omega|^2 a^\dagger a\right)^{-1} \\ &= -\sum_n \frac{1}{1+ns}|n\rangle\langle n| \end{aligned} \tag{3.1.8}$$

where $s = \frac{2|\eta\Omega|^2}{\delta_b^2 + \left(\frac{\gamma}{2}\right)^2}$ and $b \equiv \sum_n \frac{\sqrt{n+1}}{1+ns}|n\rangle\langle n+1|$. Plugging the atomic operators back into the master equation (Eq. (3) in the main text), we finally arrive at:

$$\begin{aligned}\dot{P}_n =& -\frac{\kappa}{2}(n_{\text{th}}+1)(2nP_n - 2(n+1)P_{n+1}) \\ & -\frac{\kappa}{2}n_{\text{th}}(2(n+1)P_n - 2nP_{n-1}) \\ & -\frac{\gamma s}{2}\left(\frac{n+1}{1+ns}P_n - \frac{n}{1+(n-1)s}P_{n-1}\right).\end{aligned} \tag{3.1.9}$$

In this equation, we have added the thermal contribution characterized by the noise level n_{th}, which can be estimated as $n_{\text{th}} = [\exp(\hbar\omega/k_B T) - 1]^{-1}$ [73]. In the steady-state, the probability can be computed as:

$$P_n = P_0 \prod_{k=1}^{n} \frac{\kappa n_{\text{th}} + \frac{1}{2}\frac{\gamma s}{1+(k-1)s}}{\kappa(n_{\text{th}}+1)} \tag{3.1.10}$$

where P_0 is the normalization factor such that $\sum_n P_n = 1$. And the gain can be rewritten in terms of P_n:

$$\mathcal{G} = -\gamma\frac{s}{2}\langle\sigma_z\rangle = \sum_n \frac{\gamma s}{2(1+ns)}P_n, \tag{3.1.11}$$

3.1.2 Phonon number distribution, correlation, and line narrowing

Figure 3.2 depicts the gain as a function of pumping strength in the steady state. It demonstrates the observation of lasing behavior when the gain-to-loss ratio ($\mathcal{G}/\kappa$) ap-

doi:10.6342/NTU202301896

proaches one, which occurs when the driving strength $\eta\Omega$ exceeds the threshold value of $\eta\Omega_c = 0.25\omega_0$. The time required for lasing to initiate depends on the steady-state mean phonon number $\langle n\rangle_s$. For $\langle n\rangle_s \approx 2000$, it takes approximately $14\kappa^{-1} \approx 2300\omega_0^{-1}$, equivalent to roughly 4.5 ms.

To assess the extent of lasing, we calculate the second-order correlation function $g^{(2)}(0) \equiv \left|\langle a^\dagger(0)a^\dagger(\tau)a(\tau)a(0)\rangle / \langle a^\dagger a\rangle^2\right|_{\tau=0}$ and the steady-state mean phonon number $\langle n\rangle_s$ The results are illustrated in Figure 3.2(b). Below the pumping threshold, when the pumping levels are low, $g^{(2)}_{\mathrm{ph}}(0)$ is approximately two due to the small phonon number, indicating a thermal chaotic phonon state. However, as $\eta\Omega$ exceeds $\eta\Omega_c$, the phonon number increases significantly, causing the $g^{(2)}$ curve to abruptly drop to unity. This drop signifies the emergence of a coherent state that aligns with the gain profile.

Moreover, the steady-state phonon number distribution is obtained from Eq. (3.1.9), and various profiles for different noise levels are displayed in Figure 3.2(c). At zero temperature, the distribution precisely follows the Poisson distribution. However, as the noise level rises, the distribution gradually becomes super-Poissonian, a phenomenon commonly observed in conventional optical lasers.

Additionally, we can determine the spectral lineshape of the phonon field. We start by examining the equation for the mean phonon number, given by $\frac{d\langle a^\dagger a\rangle}{dt} = \sum_n n\dot{P}_n$. By substituting Eq. (3.1.9), we obtain:

$$\frac{d}{dt}\langle n\rangle = \sum_n \left\{ \left(\frac{\gamma}{2}\frac{s}{1+n\cdot s} - \kappa \right) nP_n + \left(\kappa n_{\mathrm{th}} + \frac{\gamma}{2}\frac{s}{1+ns} \right) P_n \right\}. \tag{3.1.12}$$

Approximating n in the denominator of the summand by its instantaneous mean value $\langle n\rangle$, we can simplify the equation to:

$$\frac{d}{dt}\langle n\rangle \approx \left(\frac{\gamma}{2}\frac{s}{1+\langle n\rangle s} - \kappa \right)\langle n\rangle + \kappa n_{\mathrm{th}} + \frac{\gamma}{2}\frac{s}{1+\langle n\rangle s}. \tag{3.1.13}$$

We can identify the gain $\mathcal{G}(t) = \frac{\gamma}{2}\frac{s}{1+\langle n\rangle s}$, which is consistent with Eq. (3.1.11), except

doi:10.6342/NTU202301896

that n is taken to be the mean value. In the steady state, $\langle n\rangle \to \langle n\rangle_s$, and

$$\mathcal{G} \to \kappa\left(1-\frac{n_{\text{th}}}{\langle n\rangle_s}\right)-\frac{\gamma}{2\langle n\rangle_s}\frac{s}{1+\langle n\rangle_s s}. \tag{3.1.14}$$

On the other hand, the Langevin equation is given by

$$\dot{a}(t)=\left[\mathcal{G}-\left(\frac{\kappa}{2}+i(\omega-\nu)\right)\right]a(t)+\text{noise terms}, \tag{3.1.15}$$

where ν is the probe frequency understood as a Fourier component. Using the quantum regression theorem, we can obtain the spectral lineshape:

$$\begin{aligned} S(\nu) &= \mathcal{F}[\langle a^{\dagger}(\tau)a(0)\rangle] \\ &= \frac{\langle n\rangle_s}{(\nu-\omega)^2+\Delta\nu^2/4}, \end{aligned} \tag{3.1.16}$$

where $\Delta\nu=\kappa\frac{n_{\text{th}}}{\langle n\rangle_s}+\frac{\gamma}{2\langle n\rangle_s}\frac{s}{1+\langle n\rangle_s s}$, and $\mathcal{F}$ denotes the Fourier transform.

As depicted in Figure 3.2(d), the spectral linewidth becomes narrower when $\eta\Omega$ exceeds $\eta\Omega_c = 0.25\omega_0$ due to the significant increase in the phonon number.

3.1.3 Effect of finite size

In a smaller system with more realistic dimensions, the finite size effect becomes apparent and introduces a non-Markovian effect. This occurs when the out-coupled waves collide with the boundary and bounce back into the cavity, causing a revival of the local excitation. However, this issue can be resolved by limiting the observation time to a period shorter than the duration in which the effect occurs. For instance, in a system with $N \approx 100$, Fig. 3.3 shows the excitation dynamics of the cavity mode for an extended period of time.

We observe that the revival takes place in approximately $350f_0^{-1}$, equivalent to 0.7 ms, where $f_0 = \omega_0/(2\pi) = 0.5$ MHz. It takes about $270f_0^{-1} \sim 0.5$ ms for the system to reach the steady-state of single-mode lasing with $\langle n\rangle_s = 334$, which is shorter than

doi:10.6342/NTU202301896

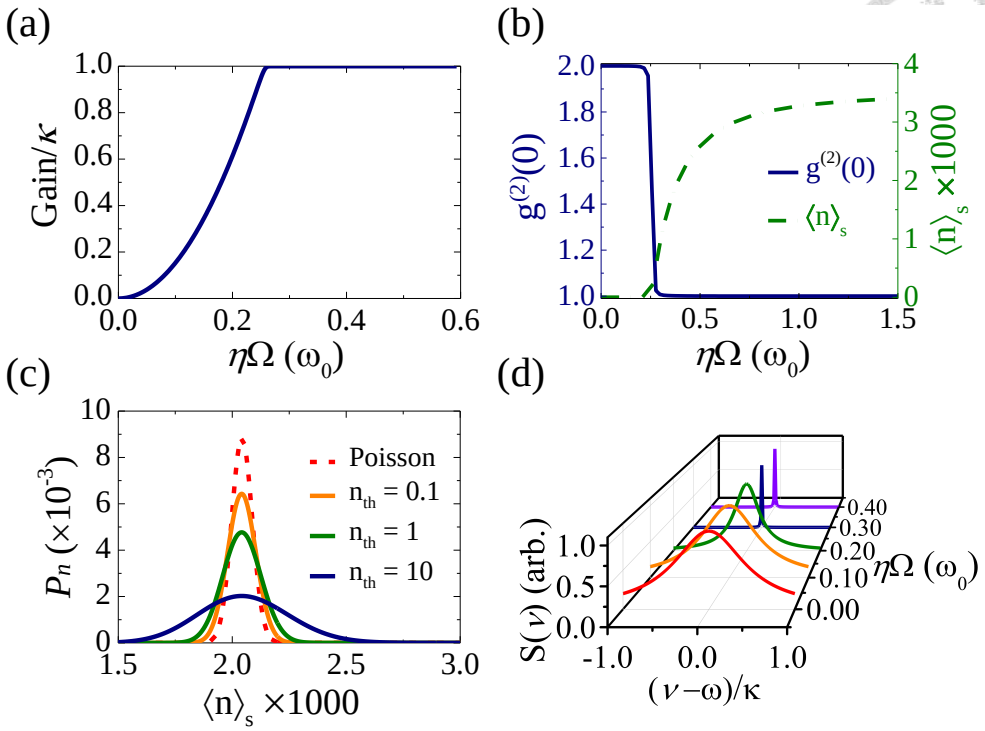

Figure 3.2: (a) The relationship between gain and driving strength is expressed in terms of $\eta\Omega$ with the blue sideband resonance $\delta_b = 0$, where the lasing threshold occurs at $\eta\Omega_c = 0.25\omega_0$. (b) The second-order correlation function $g^{(2)}$ (on the left vertical axis) and the average phonon number (on the right vertical axis) of the cavity mode are shown for various $\eta\Omega$ values. (c) The phonon number distribution is plotted for $\eta\Omega = 0.4\omega_0 = 2\pi \times 0.2$ MHz, with $\langle n \rangle_s = 2200$. (d) The spectral lineshape is presented for varied $\eta\Omega$ values, with the peak value normalized to one. For all cases (a)-(d), we select $\kappa = 6.1 \times 10^{-3}\omega_0 = 2\pi \times 3.1$ kHz based on $2+2$ tweezers of frequency $2\pi \times 2.4$ MHz, and set the cavity mode frequency to $\omega = 2.0\omega_0 = 2\pi \times 1.0$ MHz. The results in (a), (b), and (d) are all below the noise level determined by the Doppler temperature $n_{\text{th}} = 10$, which corresponding to a $^{40}Ca^{+}$ ion with a natural linewidth of $\gamma = 2\pi \times 21.6$ MHz.

the rebounded time, thereby allowing a sufficient difference in time for measurement. Notably, $\langle n \rangle_s = 334$ corresponds to a displacement of 0.3 μm, which is significantly larger than 0.05 μm, indicating the impact of thermal noise.

We proceed to compute the pertinent lasing characteristics in this scenario and graph them in Fig. 3.4. It is evident that the threshold nature endures, with the critical driving strength $\eta\Omega_c = 0.45\omega_0$. The second-order correlation function deviates slightly from unity. It is worth mentioning that this deviation is more pronounced in smaller systems compared to larger ones. Additionally, we can observe the Poissonian number distribution and profiles that broaden as the thermal levels vary.

doi:10.6342/NTU202301896

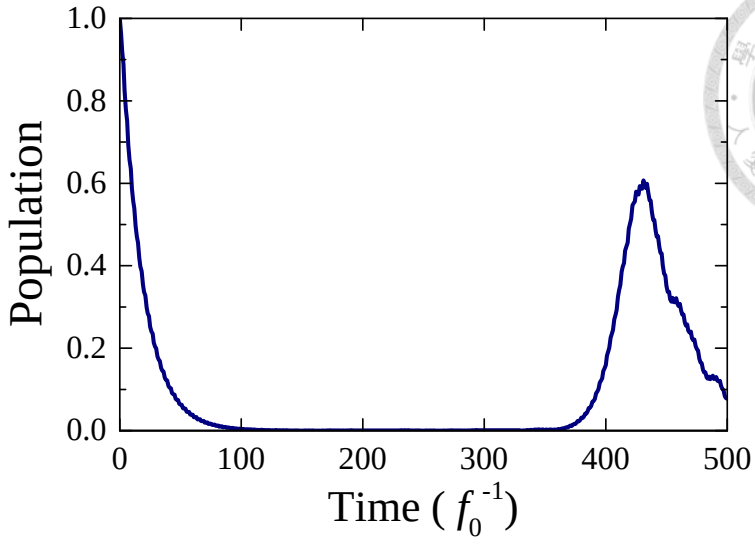

Figure 3.3: We present the relaxation and revival phenomena of the excitation in the cavity ion (the 50th ion) within an array of $N = 100$ ions. In this investigation, we choose the parameters $\kappa = 0.056\omega_0 = 2\pi \times 28.3$ kHz, which corresponds to a frequency of $1+1$ tweezers at $2\pi \times 3.0$ MHz. Furthermore, we set the cavity mode frequency to $\omega = 2.0\omega_0 = 2\pi \times 1.0$ MHz. The relaxation process occurs within the range of 0 to $100 f_0^{-1}$, while the revival occurs after $350 f_0^{-1}$.

3.2 Multi-mode phonon lasing

Let us now consider the analysis of a multimode cavity. In the context of the master-equation approach, the computational complexity of the Hilbert space increases exponentially with the number of modes and the number of phonon states after truncation serves as the base. Even for the modest value of $N_S = 2$, the computation becomes arduous for lasing phonon numbers exceeding 1000. However, certain parameters, such as mean phonon numbers and correlations, can still be calculated by utilizing the Heisenberg-Langevin equations, which employ quadrature operators $X_q \equiv a_q^\dagger + a_q$ and $P_q \equiv i(a_q^\dagger - a_q)$ for each cavity mode q. The derivation of the equations is provided in the Appendix A.2, while the results are succinctly presented in this section. It is noteworthy that this approach can be readily extended to cater to the cases where $N_S > 2$ with minor adjustments. In this regard, we have also furnished the outcomes of three and four-mode cases in the Appendix A.2.

To enhance clarity, we shall utilize the $N_S = 2$ scenario as an example, where the cavity comprises of two longitudinal collective modes: the center-of-mass (COM) mode and the

doi:10.6342/NTU202301896

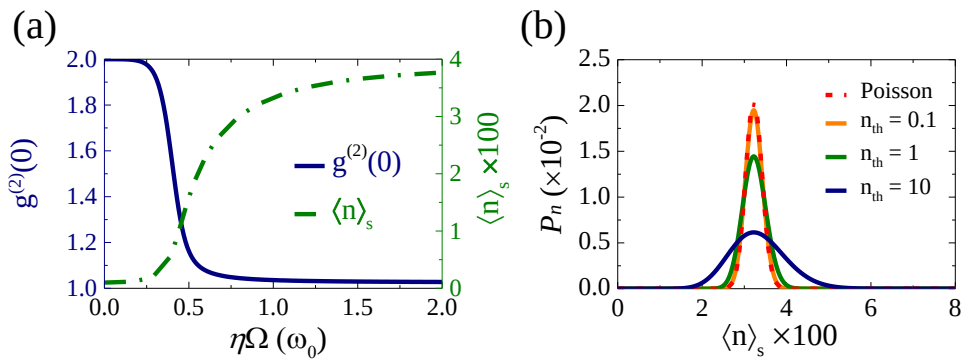

Figure 3.4: In (a), we explore the second-order correlation function, denoted as $g^{(2)}$ (on the left vertical axis), and the average phonon number (on the right vertical axis) of the cavity mode. These investigations are conducted on an array consisting of approximately $N = 100$ ions. The noise level, indicated as $n_{\text{th}} = 10$, is determined by the Doppler temperature. We vary the parameter $\eta\Omega$ to observe its effect on the correlation function and average phonon number.In (b), we analyze the phonon number statistics for different noise levels, corresponding to an average value of $\langle n\rangle_s = 334$. The pumping strength is set at $\eta\Omega = 1\omega_0 = 2\pi \times 0.5$ MHz. In this study, we employ a value of $\kappa = 0.056\omega_0 = 2\pi \times 28.3$ kHz, based on $1+1$ tweezers with a frequency of $2\pi \times 3.0$ MHz.

breathing (BR) mode, denoted by q = COM or BR. By utilizing Raman beams on one of the two ions, we stimulate the blue-sideband resonances of the cavity modes. Even though the two modes are optically distinguishable in experiments as they are separated by a few kilohertz, they can transfer energy through shared atomic excitation. This phenomenon is evident in the gain Eq. (3.1.11), where the linewidth is similar to the atomic linewidth (~ 20 MHz). Consequently, the outcome is relatively impervious to the laser detuning.

The system dynamics can be characterized by a parameter that corresponds to the classical energy associated with each mode, i.e.,

$$\mathcal{E}_q(t) \equiv \frac{1}{2}\left[\langle X_q(t)\rangle^2 + \langle P_q(t)\rangle^2\right], \tag{3.2.1}$$

which approximately represents twice the mean phonon number. To illustrate this point, we consider an example wherein we employ $w_L + w_R = 1+1$ tweezers of frequency $2\pi \times 3$ MHz, resulting in $\omega_{\text{COM}} = 1.6\omega_0$ and $\omega_{\text{BR}} = 2.5\omega_0$ with decay rates $\kappa_{\text{COM}} = 0.05\omega_0$ and $\kappa_{\text{BR}} = 0.01\omega_0$, respectively. Here, we set $\eta = \eta_{\text{COM}}$, the Lamb-Dicke parameter for the COM mode, and $\eta_{\text{BR}} = \sqrt{\omega_{\text{COM}}/\omega_{\text{BR}}}\eta$ for the BR mode. We plot the trajectories of $\mathcal{E}_q$ for a given set of lasing parameters, commencing from an initial state with specific en-

doi:10.6342/NTU202301896

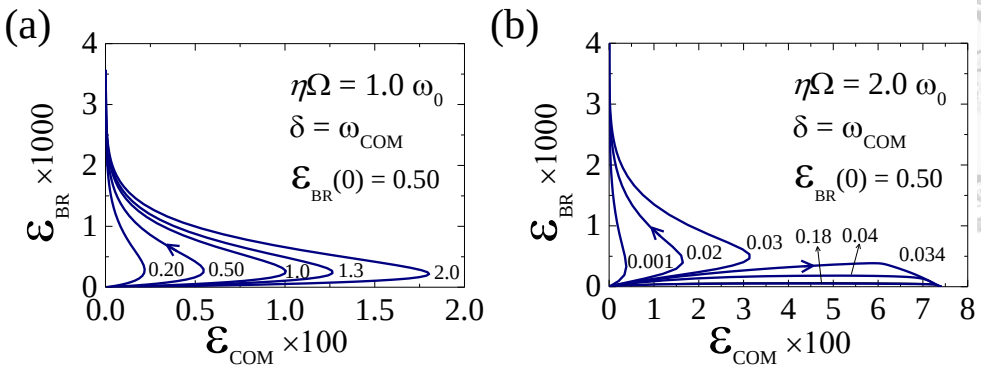

Figure 3.5: We depict the temporal trajectories of classical-energy evolution for two modes: (a) when the ratio of $\eta\Omega$ to ω_0 is 1.0, and (b) when the ratio is 2.0. Each trajectory ends at the lasing mode. In case (a), all trajectories converge to the BR mode with an average phonon number of $\langle n_{BR}\rangle_s = 1780$. In case (b), the system evolves into either the BR mode with $\langle n_{\rm BR}\rangle_s = 2050$ or the COM mode with $\langle n_{\rm COM}\rangle_s = 370$, depending on the initial distribution of $\mathcal{E}_{\rm BR}(0)$ and $\mathcal{E}_{\rm COM}(0)$. We choose the pump laser to be resonant with the COM mode's blue sideband, represented by $\delta = \omega_L - \omega_{eg} = \omega_{\rm COM}$. The associated number for each trajectory corresponds to $\mathcal{E}_{\rm COM}(0)$, while $\mathcal{E}_{\rm BR}(0) = 0.5$ remains constant. The thresholds for single-mode operation are $\eta\Omega_c^{\rm BR} = 0.4\omega_0$ for the BR mode and $\eta\Omega_c^{\rm COM} = 0.75\omega_0$ for the COM mode, provided as a reference.

ergies $(\mathcal{E}_{\rm COM}(0), \mathcal{E}_{\rm BR}(0))$. Our findings reveal that both modes cannot maintain lasing simultaneously. When lasing commences in one mode, with a significant phonon excitation, it results in the depletion of the other mode. This is evident from the evolution trajectories of classical energies, as shown in Figure 3.5(a), where the driving strength slightly exceeds both thresholds. If the system commences with low excitation, it rapidly grows and then diminishes in the COM mode, eventually reaching a steady state exclusively in the BR mode. This finding is in agreement with the single-mode calculation, which demonstrates that $\eta\Omega_c^{\rm BR} < \eta\Omega_c^{\rm COM}$, indicating that the BR mode dominates. As the driving strength increases sufficiently, the system exhibits bi-stability, where the resulting lasing mode depends on the initial excitation distribution between the two modes, as demonstrated in Figure 3.5(b).

The excitation of one mode (lasing mode) defines a phase. We construct phase diagrams for various initial classical energies and driving strengths. In Fig. 3.6, we present the phonon number curves for the COM and BR modes, respectively. As the driving strength increases, the BR mode becomes macroscopically excited when $\eta\Omega$ is greater than $\eta\Omega_c^{\rm BR}$. Even when $\eta\Omega$ is greater than $\eta\Omega_c^{\rm COM}$, the COM mode remains inactive due

doi:10.6342/NTU202301896

to competition between the modes [20]. At a driving strength of $\eta\Omega \approx 1.5\omega_0$, we observe a sharp threshold beyond which the COM mode begins to lase and immediately suppresses the BR mode. The abrupt change in phonon numbers indicates a first-order phase transition. We also calculate the second-order correlation function and obtain $g^{(2)}(0) = 1.0$ (≈ 2.0) for the lasing (non-lasing) mode, consistent with the phase diagram. Such features persist in the three- and four-mode cases.

In the ensuing discussion, we shall consider the up to four-mode case, utilizing the parameters presented in Tables 3.1 and 3.2 as examples. Additionally, we provide a list of the corresponding pumping thresholds obtained from the single-mode model to serve as a basis of comparison. It is unsurprising that the decay rate is inversely proportional to the mode frequency, and consequently, the threshold is lower. Similar to the two-mode cases, we employ classical energy as a metric to track the system's evolution. Governed by the pumping strength parameter $\eta\Omega$, the system reaches a steady state with one predominant lasing mode, indicating mode competition. However, the specific lasing mode selected is influenced by the initial mode populations in a subtle manner. Depending on the choice of initial mode populations, the lasing phase can be classified as mono-stable, bi-stable, tri-stable, or multi-stable, corresponding to the presence of one, two, three, or multiple lasing modes, respectively.

Table 3.1: Three-mode cavity mode frequency, decay rate, thermal noise, and threshold.

Mode frequency	**Decay rate**	**Thermal noise**	**Threshold**
$\omega_1 = 1.3\ \omega_0$	$\kappa_1 = 0.05\ \omega_0$	$n_{\mathrm{th},1} = 23$	$0.80\ \omega_0$
$\omega_2 = 2.1\ \omega_0$	$\kappa_2 = 0.01\ \omega_0$	$n_{\mathrm{th},2} = 13$	$0.33\ \omega_0$
$\omega_3 = 2.6\ \omega_0$	$\kappa_3 = 0.005\ \omega_0$	$n_{\mathrm{th},3} = 10$	$0.23\ \omega_0$

Table 3.2: Four-mode cavity mode frequency, decay rate, thermal noise, and threshold.

Mode frequency	**Decay rate**	**Thermal noise**	**Threshold**
$\omega_1 = 1.1\ \omega_0$	$\kappa_1 = 0.06\ \omega_0$	$n_{\mathrm{th},1} = 27$	$0.80\ \omega_0$
$\omega_2 = 1.8\ \omega_0$	$\kappa_2 = 0.02\ \omega_0$	$n_{\mathrm{th},2} = 16$	$0.46\ \omega_0$
$\omega_3 = 2.3\ \omega_0$	$\kappa_3 = 0.008\ \omega_0$	$n_{\mathrm{th},3} = 12$	$0.29\ \omega_0$
$\omega_4 = 2.6\ \omega_0$	$\kappa_4 = 0.001\ \omega_0$	$n_{\mathrm{th},4} = 11$	$0.10\ \omega_0$

Figure 3.7 depicts the mono-stable (a), bi-stable (b)(c), and tri-stable (d)-(f) cases for three cavity modes. The outcomes suggest that the mode with the highest frequency re-

doi:10.6342/NTU202301896

quires the lowest pumping threshold to initiate lasing. However, if the initial population of one mode surpasses a certain threshold, it will be compelled to lase, consequently suppressing the other modes. These characteristics remain consistent in the four-mode scenarios. Pumping strength boundaries that demarcate different multi-stabilities are furnished in Tables 3.3 and 3.4.

Table 3.3: Three-mode lasing with different pumping strengths.

Pumping strength	**Lasing mode**
$\eta\Omega \lesssim 0.85\ \omega_0$	3rd
$0.85\ \omega_0 \lesssim \eta\Omega \lesssim 2.6\ \omega_0$	2nd or 3rd
$\eta\Omega \gtrsim 2.6\ \omega_0$	All modes

Table 3.4: Four-mode lasing with different pumping strengths.

Pumping strength	**Lasing mode**
$\eta\Omega \lesssim 0.55\ \omega_0$	4th
$0.55\ \omega_0 \lesssim \eta\Omega \lesssim 1.6\ \omega_0$	3rd or 4th
$1.6\ \omega_0 \lesssim \eta\Omega \lesssim 1.8\ \omega_0$	2nd, 3rd, or 4th
$\eta\Omega \gtrsim 1.8\ \omega_0$	All modes

3.3 Chapter summary

In this chapter, we leverage the phonon cavity introduced in the previous chapter to realize a phonon laser. To achieve this, we employ a method similar to that used in Raman lasers, where an optical laser is applied to the motional blue sideband of the ions. We then explore both single mode and multimode phonon lasers.

In the context of the single mode phonon laser, we analyze various laser properties, such as threshold behavior, whether the second-order correlation function $g^{(2)}(0)$ equals 1, the nature of the phonon distribution (Poisson distribution or otherwise), and linewidth narrowing. Additionally, we consider more practical scenarios, such as cases where the number of ions is approximately 100, leading to phonon rebounded effects. Consequently, we investigate that the time required for the phonon laser to reach a steady state ($270 f_0^{-1} \sim$ 0.5 ms) is less than the rebounded time ($350 f_0^{-1} \sim 0.7$ ms).

In the multimode case, due to an abundance of adjustable parameters, we adopt the

doi:10.6342/NTU202301896

Heisenberg-Langevin approach to investigate the presence of laser mode competition. Under the two-mode case, we establish a laser phase diagram to distinguish which initial conditions give rise to specific lasing modes. For the three-mode case, we plot the temporal evolution of various initial conditions concerning different interaction strength and classical energies. We observe that when $\eta\Omega < 0.8\omega_0$, only the zig-zag mode undergoes lasing. As the interaction strength increases, lasing is also observed in the breathing mode for $1.5\omega_0 < \eta\Omega = 2.7\omega_0$, and when $\eta\Omega > 2.7\omega_0$, all modes become potential candidates for lasing. In the four-mode case, we identify the interaction strength that leads to the formation of specific lasing modes.

doi:10.6342/NTU202301896

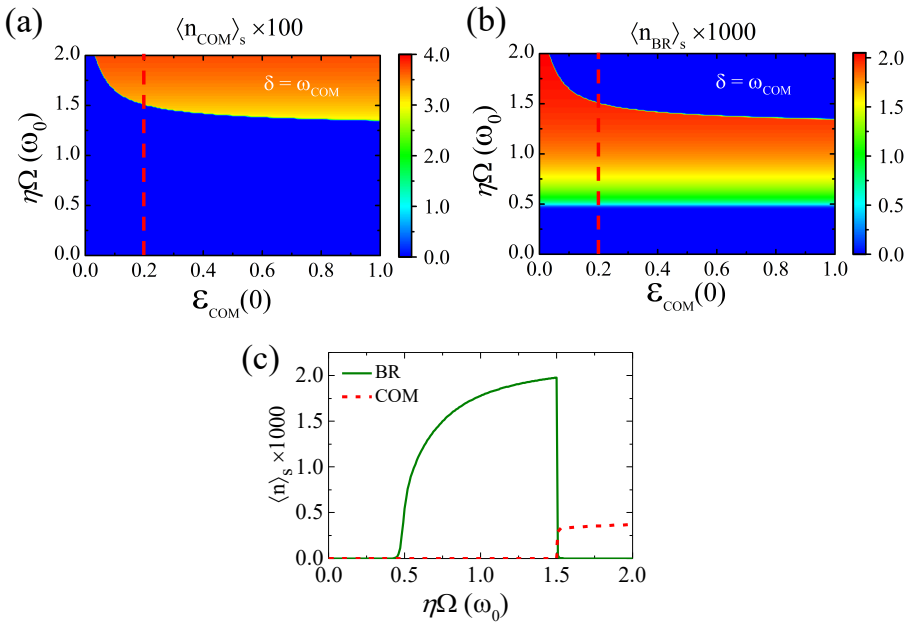

Figure 3.6: (a) The phase diagram of the COM mode in the steady-state is presented for different phonon numbers and driving strengths, denoted as $\eta\Omega$.(b) Similarly, the steady-state phase diagram of the BR mode is depicted for various phonon numbers and driving strengths, denoted as $\eta\Omega$. The initial phonon number of the BR mode is set as $\mathcal{E}_{\mathrm{BR}}(0) = 0.5$, and $\delta = 1.0\omega_{\mathrm{COM}}$.(c) The variation of phonon numbers for each mode with respect to the driving strength is shown along the line cut in (a) and (b). The phonon number of the non-lasing mode is comparable to the thermal level, where $n_{\mathrm{th,COM}} = 13$ or $n_{\mathrm{th,BR}} = 8.2$. Moreover, we observe that the BR phase emerges when the driving strength exceeds the threshold $\eta\Omega_c^{\mathrm{BR}} \approx 0.4\omega_0$, as determined by the single-mode calculation. A distinct boundary is observed at $\eta\Omega \approx 1.5\omega_0$ (significantly larger than $\eta\Omega_c^{\mathrm{COM}} \approx 0.75\omega_0$), beyond which the lasing phase transitions to the COM mode.(c) The variation of phonon numbers for each mode with respect to the driving strength is shown along the line cut in (a) and (b). The phonon number of the non-lasing mode is comparable to the thermal level, where $n_{\mathrm{th,COM}} = 13$ or $n_{\mathrm{th,BR}} = 8.2$. Moreover, we observe that the BR phase emerges when the driving strength exceeds the threshold $\eta\Omega_c^{\mathrm{BR}} \approx 0.4\omega_0$, as determined by the single-mode calculation. A distinct boundary is observed at $\eta\Omega \approx 1.5\omega_0$ (significantly larger than $\eta\Omega_c^{\mathrm{COM}} \approx 0.75\omega_0$), beyond which the lasing phase transitions to the COM mode.

doi:10.6342/NTU202301896

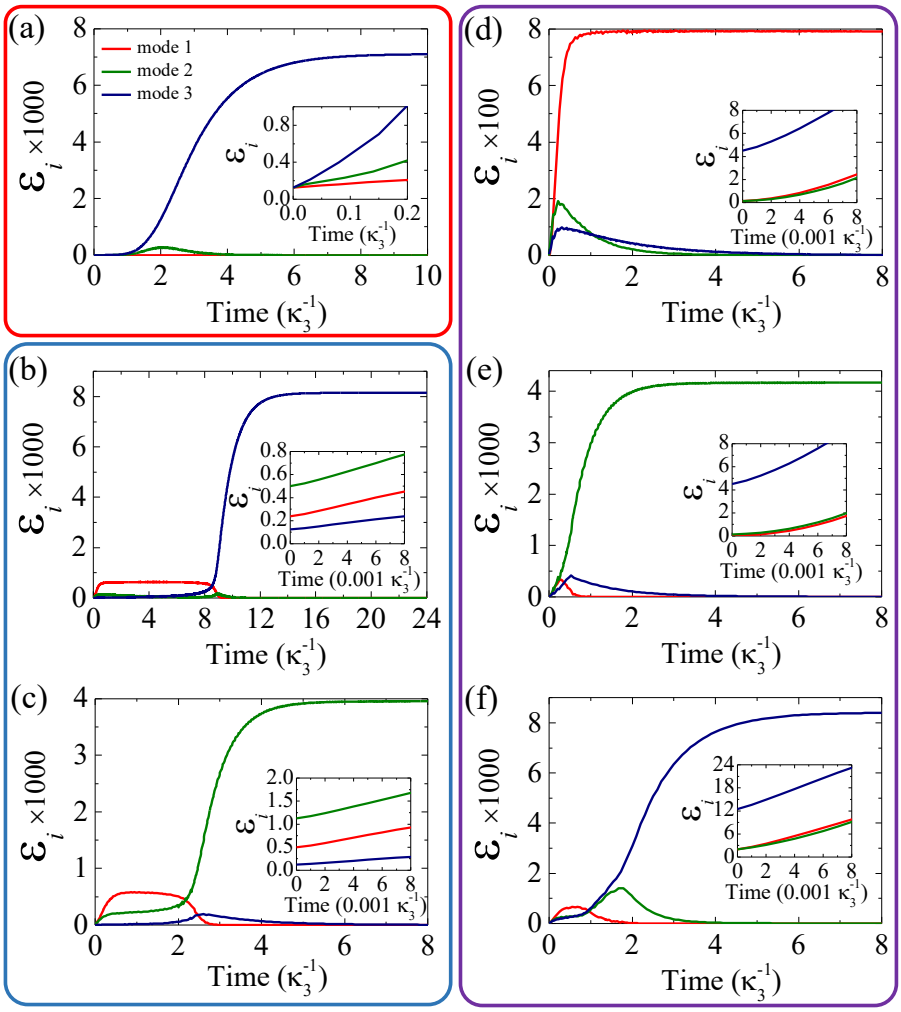

Figure 3.7: The figure presents the temporal evolution of the three modes under different conditions: (a) for $\eta\Omega = 0.8\omega_0$, (b) and (c) for $\eta\Omega = 1.5\omega_0$, and (d) to (f) for $\eta\Omega = 2.7\omega_0$, all with a detuning of $\delta = \omega_1$. The inset displays the corresponding curves of $\mathcal{E}_{i=1,2,3}$.

doi:10.6342/NTU202301896

doi:10.6342/NTU202301896

Chapter 4

EIT cooling with an ion crystal assisted by optical tweezers

EIT cooling is a highly effective sub-Doppler cooling technique utilized in trapped systems to achieve motional ground-state cooling of trapped ions. This cooling is a crucial requirement in the domains of quantum computing and quantum simulation.

In systems comprising of a large array of ions, the spectral complexity of the motional structure is significantly amplified, resulting in an intricate resolution process. Consequently, the cooling process faces daunting challenges that increase proportionally with the number of ions.

The upcoming chapter seeks to investigate the cooling limitations and cooling rates achievable in multimode cavities containing a sizeable ion crystal and optical tweezers.

4.1 Cooling in an ion crystal

In a one-dimensional ion crystal, researchers have successfully employed the technique of EIT cooling to bring each radial mode of the crystal, composed of 18 $^{40}Ca^{+}$ ions, to its motional ground state [2]. In their experimental setup, they select the Zeeman sublevels of the $S_{1/2} \Longleftrightarrow P_{1/2}$ dipole transition at 397 nm to serve as a three-level system, as depicted in Fig 4.1. The σ^{+}-polarized beam is employed to facilitate a strong coupling between the ground state $\left|S_{1/2}, m = -1/2\right\rangle$ and the excited state $\left|P_{1/2}, m = 1/2\right\rangle$, thereby

doi:10.6342/NTU202301896

inducing the formation of dressed states. A π-polarized beam serves as the probe beam, enabling cooling effects to be achieved. However, in their experiment, polarization imperfections (σ^--polarized beam) will give rise to additional heating processes. Due to the spontaneous decay of the $|P_{1/2}\rangle$ state to the $|D_{3/2}\rangle$ state, an additional laser at 866 nm is required to bring the state back to the $|P_{1/2}\rangle$ state. To probe the system's temperature, the quadrupole transition $S_{1/2} \Longleftrightarrow D_{5/2}$ can be utilized. The lifetime of the $|D_{5/2}\rangle$ state, which is approximately 1.1 seconds, is reduced when laser light at 854 nm is applied. This laser light couples the metastable state to the short-lived $|P_{3/2}\rangle$ state. The read-out of the electronic state of the ions is achieved through the electron-shelving method, employing either a photomultiplier tube or an electron-multiplying charged coupled device camera. This method allows for the measurement of both the total and individual states of the ions.

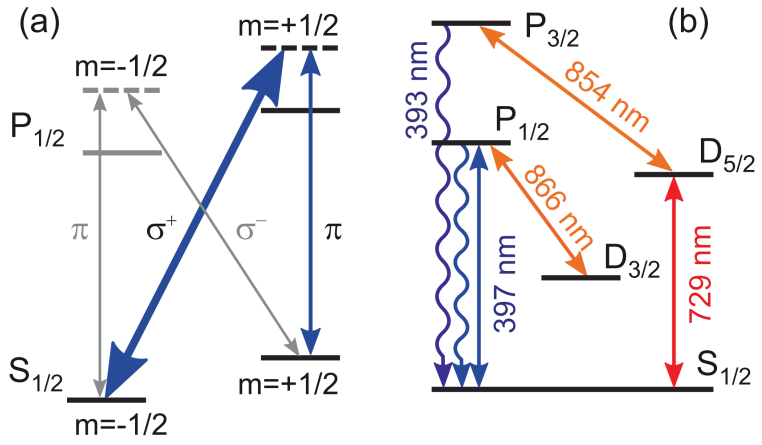

Figure 4.1: (a, b) The experiment utilizes a schematic of the $^{40}Ca^+$ transitions. EIT cooling is achieved through the implementation of the Zeeman sublevels of the $S_{1/2} \Longleftrightarrow P_{1/2}$ dipole transition. The dipole-allowed transitions used for Doppler cooling, detection, and quenching are driven by light at 397 nm, 866 nm, and 854 nm, respectively, while the quadrupole transition utilized for motional state analysis is driven by light at 729 nm. (retrieved from Ref.[2])

Through the aforementioned experimental approach, they were able to cool the radial modes of the ion crystal, consisting of 9 and 18 ions, to an average phonon number ranging from approximately 0.01 to 0.02. The ability to cool to such low temperatures in radial modes can be attributed to the fact that the width of the radial mode spectrum is smaller

doi:10.6342/NTU202301896

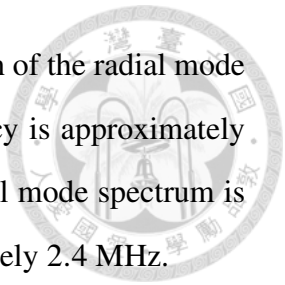

than its mean mode frequency. In the case of a 9-ion crystal, the width of the radial mode spectrum is approximately 1.2 MHz, while the mean mode frequency is approximately 2.2 MHz. Similarly, in the 18-ion crystal case, the width of the radial mode spectrum is approximately 0.8 MHz, and the mean mode frequency is approximately 2.4 MHz.

In addition, in this paper, they were able to cool all modes of the 2-ion crystal, including axial and radial modes, to their motional ground state. However, simultaneously cooling all modes using a single EIT cooling method poses a challenge due to the fact that the frequencies of axial modes (1.13 MHz for the COM mode and 1.96 MHz for the stretch mode) are lower than the frequencies of radial modes (ranging from 3.09 to 3.84 MHz).

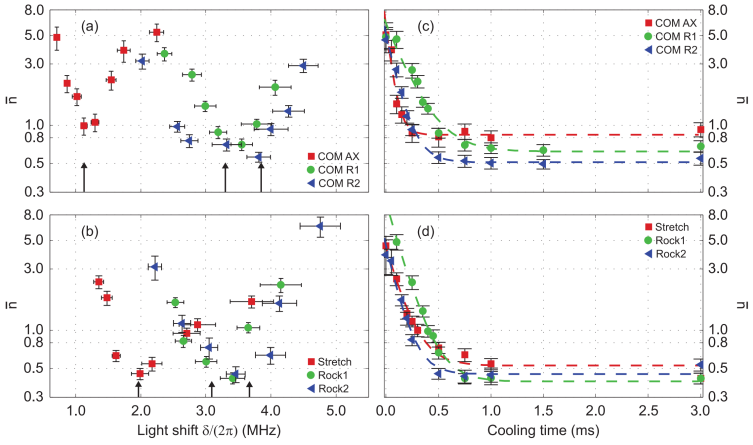

Figure 4.2: (a) The cooling range of the COM mode. (b) The cooling range of the stretch mode and rock mode. (c, d) The temporal evolution of moth modes. (retrieved from Ref.[2])

4.2 Model of the system

We consider a multimode phonon cavity, which consists of a large uniform ion crystal and optical tweezers (Fig. 3.1). We apply the EIT cooling to the phonon cavity. To investigate whether the out-coupled field helps for taking out the local phonon or thermally exciting,

doi:10.6342/NTU202301896

we derive a rate equation

$$\begin{aligned}\dot{P}_{n_k} = & A_{k-}\left[(n_k+1)P_{n_k+1} - n_k P_{n_k}\right] \\ & + A_{k+}\left[n_k P_{n_k-1} - (n_k+1)P_{n_k}\right] \\ & + \kappa_k\left\{(n_{\mathrm{th},k}+1)\left[(n_k+1)P_{n_k+1} - n_k P_{n_k}\right]\right. \\ & \left. + n_{\mathrm{th},k}\left[n_k P_{n_k-1} - (n_k+1)P_{n_k}\right]\right\}, \end{aligned} \tag{4.2.1}$$

where η_k is the Lamb-Dicke parameter, κ_k is the motional mode decay rate, and $n_{\mathrm{th},k}$ is the thermal noise from the out-coupled field and can be evaluated by $[\exp(\hbar\omega_k/k_B T_d)-1]^{-1}$ with the collective motional mode frequencies ω_k and a Doppler temperature T_d. The coefficients $A_{k\pm}$ have the form

$$A_{k\pm} = \frac{\eta_k^2}{4}\left(\frac{\Omega_c\Omega_p}{\Omega}\right)^2 \frac{\gamma\omega_k^2}{\left[\Omega^2/4 - \omega_k(\omega_k \mp \Delta)\right]^2 + \gamma^2\omega_k^2/4}, \tag{4.2.2}$$

where Ω, $\Omega_c\,(\Omega_p)$, γ, and Δ are $\sqrt{\Omega_c^2+\Omega_p^2}$, the Rabi frequency of control (probe) beam, the atomic transition linewidth, and the detuning, respectively. From Eq. (4.2.1), one can obtain the dynamical evolution of the mean phonon number

$$\langle \dot{n}_k \rangle = -W_k \langle n_k \rangle + A_{k+} + \kappa_k n_{\mathrm{th},k}, \tag{4.2.3}$$

where W_k is the cooling rate and has a form $W_k = A_{k-} - A_{k+} + \kappa_k$. The steady-state mean phonon number is given by

$$\langle n_k \rangle_{\mathrm{ss}} = \frac{A_{k+} + \kappa_k n_{\mathrm{th},k}}{A_{k-} - A_{k+} + \kappa_k}. \tag{4.2.4}$$

Firstly, we are only considering an ion crystal formed by 10 ions. We have observed that each mode has the potential to reach its own motional ground state (see Fig. 4.3). However, due to the significant differences in detuning (δ) for each mode, simultaneously cooling all of them is challenging.

doi:10.6342/NTU202301896

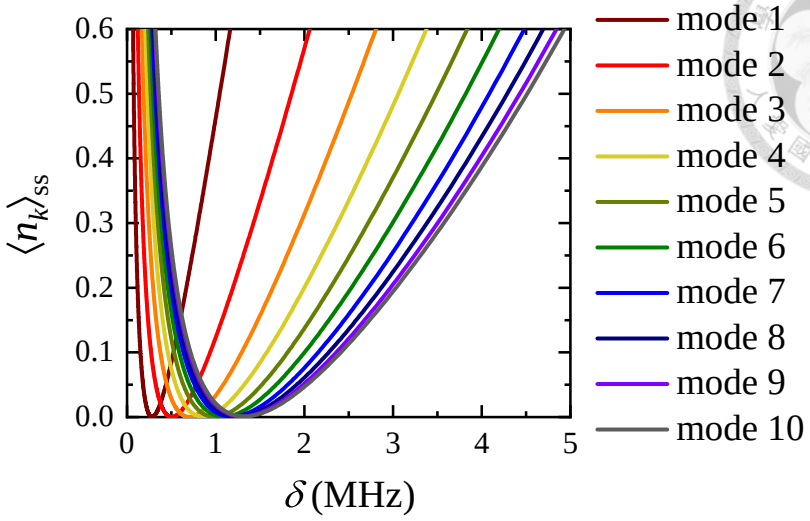

Figure 4.3: The reaction of steady-state mean phonon number with different choices of the detuning δ. The ion species what we choose is $^{40}Ca^{+}$. According to the experimental achievable parameters, the Rabi frequencies of the coupling field and the probe field are $\Omega_c = 2\pi \times 30$ MHz and $\Omega_p = 2\pi \times 6.2$ MHz [2]. According to their frequencies, the collective normal modes are arranged in the following order (1: lowest; 10: highest).

In order to simultaneously cool each mode, we propose the utilization of multiple EIT cooling techniques. Therefore, the coefficients $A_{k\pm}$ need to be redefined as $A_{k\pm} = \sum_i A_{i,k\pm}$, with i denoting the number of cooling beams employed.

To begin, we define a quantity $L_{total} = \sum_k \sqrt{\frac{(2\langle n_k \rangle_{ss}+1)\hbar}{2m\omega_k}}$, which represents the total displacement of ions. Subsequently, we optimize this parameter.

Figure 4.4 illustrates that the majority of modes exhibit improvements as the EIT cooling number increases.

4.3 Effective cooling rate and cooling limit

For the purpose of investigating how the decay rate κ_k influences the steady-state mean phonon $\langle n_k \rangle_{ss}$ and the effective cooling rate W_k, we plot the result in Fig. 4.5. It shows that the steady-state mean phonon number does not decrease as the decay rate increases despite growing the effective cooling rate. The main reason of the issue is that the cooling rate of the EIT cooling is too weak compare to the decay rate.

doi:10.6342/NTU202301896

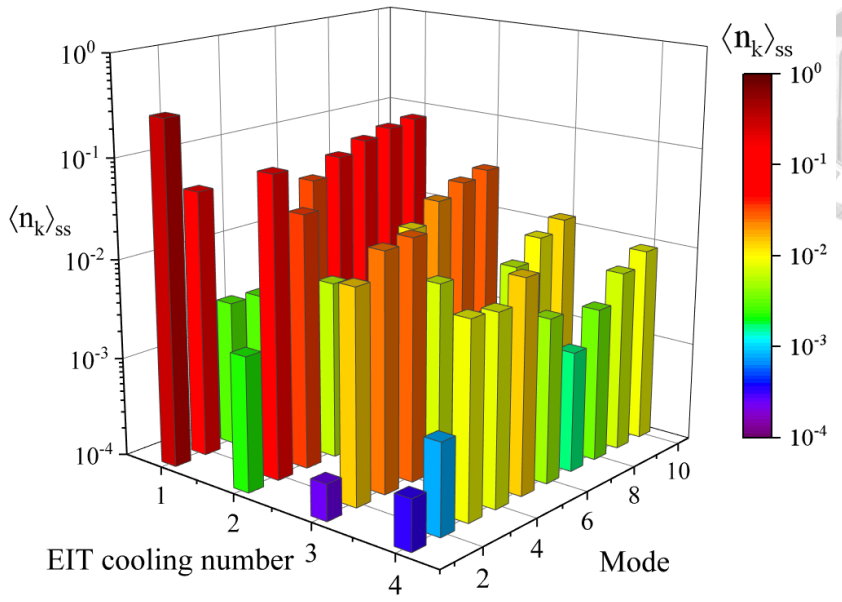

Figure 4.4: The steady-state mean phonon number for 10 modes with different EIT cooling numbers.

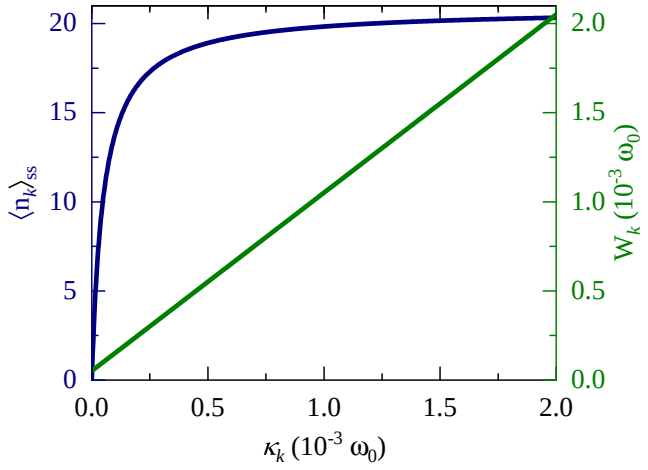

Figure 4.5: The cooling limit and the effective cooling rate for $\omega_k = 1\omega_0$ with different decay rate. The Rabi frequencies are the same in Fig. 4.3

To deal with the issue, We utilized the methodologies introduced in the previous section to achieve improvements in both the steady-state mean phonon number and the effective cooling rate. Figure 4.6 clarifies that increasing EIT cooling numbers not only cool down the steady-state phonon number but also rise the cooling rate for 10 modes. The ranges of motional frequencies are

doi:10.6342/NTU202301896

$\omega_k = 0.3 \sim 1.4$ MHz.

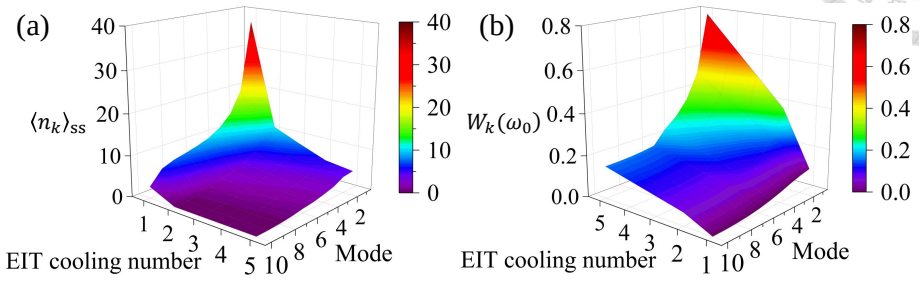

Figure 4.6: (a) The steady-state mean phonon number and (b) the effective cooling rate for 10 modes with different EIT cooling numbers. The decay rates are the same in Fig. 3.3. The collective normal modes are ordered the same in Fig. 4.3. The Rabi frequencies are the same in Fig. 4.5

4.4 Chapter summary

In this chapter, we reviewed how previous researchers cooled 9 and 18 $^{40}Ca^{+}$ ions forming an ion crystal to its motional ground state in the radial mode. They were able to successfully cool down all the radial modes, but they encountered some challenges when attempting to cool down all the motional modes in the 2-ion crystal. The significant difference in frequencies between the axial and radial modes limited the cooling capabilities.

Later, we considered our system, we derived the formula for EIT cooling in the phonon cavity. To assess the feasibility of our derived formula and to anticipate potential challenges, we focused on a 10-ion crystal. We observed that each axial mode could be cooled to its motional ground state individually. However, cooling all modes simultaneously to their motional ground states proved to be impossible due to the excessively wide cooling range. Therefore, we proposed employing multiple EIT coolings as a solution to address this issue.

Next, we considered applying EIT cooling to our proposed phonon cavity. Unfortunately, we encountered difficulties in cooling the ions effectively due to the influence of out-coupled ions. Addressing the aforementioned issues, by implementing multiple EIT

doi:10.6342/NTU202301896

cooling techniques, we endeavored to address the challenges effectively. As a result, both the cooling limit and the cooling rate showed significant improvements.

we proposed increasing the number of EIT cooling processes to tackle the problem. Remarkably, we found that increasing the number of EIT cooling processes resulted in improved cooling limits and rates for each mode.

doi:10.6342/NTU202301896

Chapter 5

Conclusion and outlook

5.1 Conclusion

In this study, we propose a prototype for a tunable phonon laser using a large array of trapped ions. By employing optical tweezers, we effectively immobilize a subset of ions to emulate an acoustic cavity, serving as a resonator for phonon lasing. Our investigation begins by examining the Markovian nature of the phonon cavity. We adjust the intensity of the optical tweezers and observe the real-time evolution of phonons to determine the additivity of decay rates, thereby validating our proposed model.

Next, we utilize Raman lasers technique to achieve phonon lasing. By employing a blue sideband transition with significantly higher damping of the internal state compared to the phonon's degrees of freedom, we effectively create a phonon laser. We analyze the lasing characteristics in the single-mode regime, including threshold behavior, the second-order correlation function unity, Poisson distribution, and linewidth narrowing.

To address a more realistic scenario, we consider an ion array consisting of approximately 100 ions. Due to the finite-size nature of the system, this introduces non-Markovian effects. To mitigate this, we limit our analysis to a time span shorter than the duration required for non-Markovianity to manifest.

Furthermore, we explore multimode phonon lasing, extending our investigation up to four-mode lasing. We observe mode competition and demonstrate the system's multistability under different initial conditions.

doi:10.6342/NTU202301896

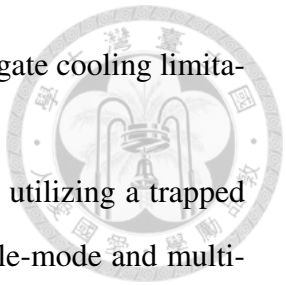

Lastly, we incorporate EIT cooling into this architecture to investigate cooling limitations and cooling rates.

In summary, our study presents a tunable phonon laser prototype utilizing a trapped ion array. We examine the Markovianity of the system, achieve single-mode and multi-mode phonon lasing, and explore the cooling limitations and rates through EIT cooling.

5.2 Outlook

Strictly speaking, the presence of phonon reflections prevents our system from being classified as Markovian. Moreover, the real-time evolution approach is inconvenient for observing the behavior of the phonon. Therefore, it is crucial to ascertain the associated noise spectrum as it pertains to the properties of the bath. Once the noise spectrum is determined, it may be possible to develop a more comprehensive framework for phonon lasers, specifically focusing on non-Markovian phonon lasers. In order to approximate a Markovian environment, laser cooling can be employed to effectively suppress phonon reflections, thereby establishing an ideal Markovian setting. Additionally, laser-induced techniques like bath engineering offer the potential to create intriguing environments with unique characteristics.

doi:10.6342/NTU202301896

doi:10.6342/NTU202301896

doi:10.6342/NTU202301896

Appendix A

Derivation

A.1 Dispersion of an ion crystal

To comprehend the physical behavior of this system, including the phase velocity and group velocity in the proposed phonon cavity, we must first understand the dispersion relation. The force equation that governs the system is as follows:

$$\ddot{y}_i = \sum_j A_{ij} y_j,$$

where $A_{ii} = A = \omega_\xi^2 + 2C\zeta(3)$, $A_{ij} = A_{n=|j-i|} = -\frac{C}{|n|^3}$, and $C = 2$ for longitudinal modes and $C = -1$ for transverse modes. The value $\zeta(3) \approx 1.2$ represents the Riemann zeta function evaluated at 3, which is also equivalent to the polylogarithm function $PolyLog(3,1) \equiv Li_3(1)$. Additionally, in the case of an infinitely long array, the angular frequencies for transverse and longitudinal modes are $\omega_{\xi=\text{trans}} = \omega_T$ and $\omega_{\xi=\text{longi}} = 0$.

Let us examine a system described by the equation $y_i = e^{i(kx_i - \omega t)}$, where $k = \frac{2\pi}{\lambda} d_0$, x_i, and ω are dimensionless quantities, utilizing units of the ion spacing d_0 and the characteristic frequency ω_0. In this context, x_i represents integer values, denoting discrete spatial positions.

Now, we proceed to express $\omega^2 y$ in terms of y_i by applying the relation $y_{i+n} = e^{ikn} y_i$. Substituting this relation, we obtain:

$$\omega^2 y = \cdots + A_2 y_{-2} + A_1 y_{-1} + A y + A_1 y_1 + A_2 y_2 + \cdots .$$

doi:10.6342/NTU202301896

Next, we aim to determine the dispersion relation by expressing A and A_n in terms of k:

$$\begin{aligned}\omega^2 =& A + 2\sum_{n=1}^{\infty} A_n \cos kn \\ =& A - 2C\sum_{n=1}^{\infty} \frac{\cos kn}{n^3} \\ =& A - C\left(\mathrm{Li}_3(e^{ik}) + \mathrm{Li}_3(e^{-ik})\right).\end{aligned} \tag{A.1.1}$$

Hence, the phase velocity v(k) of the phonon can be obtained as follows:

$$v_p(k) = \frac{\omega}{k} = \frac{\sqrt{A - C\left(\mathrm{Li}_3(e^{ik}) + \mathrm{Li}_3(e^{-ik})\right)}}{k}.$$

Additionally, we can employ numerical methods to calculate $v_p(\omega)$ for further analysis. Furthermore, we can compute the group velocity $v_g(\omega) = \frac{d\omega}{dk}$ using numerical techniques to gain deeper insights into the system's characteristics.

Using longitudinal waves as an example, Fig. A.1(a) illustrates that when the frequency exceeds $2.9\omega_0$, no corresponding phase velocity can be attained. This implies that phonons are unable to propagate out of the cavity. Moreover, as depicted in Fig. A.1(b), with an increase in frequency, the phonon group velocity decreases. This observation supports Fig. 2.2, which demonstrates that higher-frequency phonons correspond to lower decay rates.

A.2 Model for phonon lasing - multimode

The approach described in Section 3.1.9, known as the rate equation approach, can also be applied to multi-mode cavities. However, due to the exponential growth in the dimension of the required Hilbert space with the number of modes, the calculation becomes intractable even for $N_S = 2$. In this case, an alternative method based on the normal-mode

doi:10.6342/NTU202301896

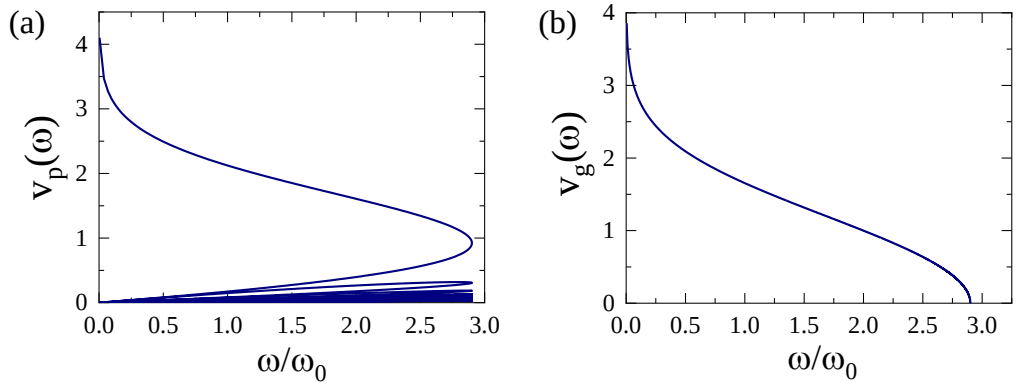

Figure A.1: (a) The phase velocity $v_p(\omega)$ and (b) group velocity $v_g(\omega)$ vary with different frequencies.

quadrature operators is adopted [25].

The Hamiltonian that describes the multi-mode phonon cavity is given by:

$$H/\hbar = -\frac{\delta}{2}\sigma_i^z + \sum_q \omega_q a_q^\dagger a_q + \sum_{i,q} c_q \eta_q \Omega_i \left(\sigma_i^+ a_q^\dagger + a_q \sigma_i^-\right) \tag{A.2.1}$$

Here, δ represents the difference between the laser frequency ω_L and the energy transition frequency ω_{eg}. The operators a_q and $a_q^\dagger$ are the phonon field operators for the qth cavity mode, while σ_i^- and σ_i^+ are atomic operators for the ith atom, driven by a laser with frequency ω_L and Rabi frequency Ω_i. The coefficient c_q corresponds to the qth mode and is determined by the eigenvectors of matrix $\mathbf{A}_C$. Additionally, η_q represents the Lamb-Dicke parameter for the qth mode.

The normal-mode quadrature operators are defined as:

$$\begin{cases} X_q = a_q^\dagger + a_q \\ P_q = i\left(a_q^\dagger - a_q\right). \end{cases} \tag{A.2.2}$$

Using these operators, the Langevin equations for the quadrature operators of different orders are given by:

doi:10.6342/NTU202301896

$$\begin{aligned}\frac{d}{dt}\left(P_q^n X_q^m\right) =& -n\omega_q\left(P_q^{n-1}X_q^{m+1} + i\,(n-1)\,P_q^{n-2}X_q^m\right)\\ &+ m\omega_q\left(P_q^{n+1}X_q^{m-1} + i\,(m-1)\,P_q^n X_q^{m-2}\right)\\ &-\frac{1}{2}\kappa_q n P_q^n X_q^m + \frac{1}{2}\kappa_q\left(2n_{\mathrm{th},q}+1\right)\left(n\,(n-1)\,P_q^{n-2}X_q^m\right)\\ &-\frac{1}{2}\kappa_q m P_q^n X_q^m + \frac{1}{2}\kappa_q\left(2n_{\mathrm{th},q}+1\right)\left(m\,(m-1)\,P_q^n X_q^{m-2}\right)\\ &- n\sum_{i,q} c_q\eta_q\Omega_i\left(\sigma_i^- + \sigma_i^+\right)P_q^{n-1}X_q^m\\ &- im\sum_{i,q} c_q\eta_q\Omega_i\left(\sigma_i^- - \sigma_i^+\right)P_q^n X_q^{m-1}, \end{aligned} \tag{A.2.3}$$

The equations for the time evolution of the atomic operators are:

$$\frac{d}{dt}\sigma_i^- = \left(i\delta - \frac{\gamma}{2}\right)\sigma_i^- + i\frac{1}{2}\sum_q c_q\eta_q\Omega_i\sigma_{z,i}\left(X_q - iP_q\right), \tag{A.2.4}$$

$$\frac{d}{dt}\sigma_{z,i} = -\gamma\left(\sigma_{z,i}+1\right) - i\sum_q c_q\eta_q\Omega_i\left(\sigma_{z,i}^+\left(X_q - iP_q\right) - \mathrm{H.c.}\right) \tag{A.2.5}$$

It is important to note that different modes decay independently but are still coupled through the sharing of atomic states, as shown by the last terms of equations (A.2.4) and (A.2.5). The second-order correlation function, denoted as $g_q^{(2)}(0)$, can be directly calculated using the formula: $g_q^{(2)}(0) = \left(\left\langle n_q^2\right\rangle - \left\langle n_q\right\rangle\right)/\left\langle n_q\right\rangle^2$

where

$$\left\langle n_q\right\rangle = \frac{1}{4}\left(\left\langle X_q^2\right\rangle + \left\langle P_q^2\right\rangle\right) - \frac{1}{2} \tag{A.2.6}$$

and

doi:10.6342/NTU202301896

$$\langle n_q^2 \rangle = \frac{1}{16}\left(\langle X_q^4 \rangle + \langle P_q^4 \rangle + 2Re\langle P_q^2 X_q^2 \rangle\right) - \frac{1}{4}\left(\langle X_q^2 \rangle + \langle P_q^2 \rangle + 2Im\langle P_q X_q \rangle + 1\right). \quad \text{(A.2.7)}$$

doi:10.6342/NTU202301896

doi:10.6342/NTU202301896

Bibliography

[1] Y.-C. Shen and G.-D. Lin, "Scalable quantum computing stabilised by optical tweezers on an ion crystal," *New Journal of Physics*, vol. 22, p. 053032, May 2020.

[2] R. Lechner, C. Maier, C. Hempel, P. Jurcevic, B. P. Lanyon, T. Monz, M. Brownnutt, R. Blatt, and C. F. Roos, "Electromagnetically-induced-transparency ground-state cooling of long ion strings," *Physical Review A*, vol. 93, p. 053401, may 2016.

[3] R. Blatt and D. Wineland, "Entangled states of trapped atomic ions," *Nature*, vol. 453, pp. 1008–1015, jun 2008.

[4] C. Monroe and J. Kim, "Scaling the ion trap quantum processor," *Science*, vol. 339, pp. 1164–1169, mar 2013.

[5] T. Harty, D. Allcock, C. Ballance, L. Guidoni, H. Janacek, N. Linke, D. Stacey, and D. Lucas, "High-fidelity preparation, gates, memory, and readout of a trapped-ion quantum bit," *Physical Review Letters*, vol. 113, p. 220501, nov 2014.

[6] C. Ballance, T. Harty, N. Linke, M. Sepiol, and D. Lucas, "High-fidelity quantum logic gates using trapped-ion hyperfine qubits," *Physical Review Letters*, vol. 117, p. 060504, aug 2016.

[7] J. Gaebler, T. Tan, Y. Lin, Y. Wan, R. Bowler, A. Keith, S. Glancy, K. Coakley, E. Knill, D. Leibfried, and D. Wineland, "High-fidelity universal gate set for 9be+ ion qubits," *Physical Review Letters*, vol. 117, p. 060505, aug 2016.

doi:10.6342/NTU202301896

[8] M. Um, J. Zhang, D. Lv, Y. Lu, S. An, J.-N. Zhang, H. Nha, M. S. Kim, and K. Kim, "Phonon arithmetic in a trapped ion system," *Nature Communications*, vol. 7, apr 2016.

[9] S. An, J.-N. Zhang, M. Um, D. Lv, Y. Lu, J. Zhang, Z.-Q. Yin, H. T. Quan, and K. Kim, "Experimental test of the quantum jarzynski equality with a trapped-ion system," *Nature Physics*, vol. 11, pp. 193–199, dec 2014.

[10] H. Gan, G. Maslennikov, K.-W. Tseng, C. Nguyen, and D. Matsukevich, "Hybrid quantum computing with conditional beam splitter gate in trapped ion system," *Physical Review Letters*, vol. 124, p. 170502, apr 2020.

[11] K. Vahala, M. Herrmann, S. Knünz, V. Batteiger, G. Saathoff, T. W. Hänsch, and T. Udem, "A phonon laser," *Nature Physics*, vol. 5, pp. 682–686, Sep 2009.

[12] S. Knünz, M. Herrmann, V. Batteiger, G. Saathoff, T. W. Hänsch, K. Vahala, and T. Udem, "Injection locking of a trapped-ion phonon laser," *Phys. Rev. Lett.*, vol. 105, p. 013004, Jul 2010.

[13] M. Ip, A. Ransford, A. M. Jayich, X. Long, C. Roman, and W. C. Campbell, "Phonon lasing from optical frequency comb illumination of trapped ions," *Phys. Rev. Lett.*, vol. 121, p. 043201, Jul 2018.

[14] J. Kabuss, A. Carmele, T. Brandes, and A. Knorr, "Optically driven quantum dots as source of coherent cavity phonons: A proposal for a phonon laser scheme," *Phys. Rev. Lett.*, vol. 109, p. 054301, Jul 2012.

[15] J. Kabuss, A. Carmele, and A. Knorr, "Threshold behavior and operating regimes of an optically driven phonon laser: Semiclassical theory," *Phys. Rev. B*, vol. 88, p. 064305, Aug 2013.

[16] A. Khaetskii, V. N. Golovach, X. Hu, and I. Žutić, "Proposal for a phonon laser utilizing quantum-dot spin states," *Phys. Rev. Lett.*, vol. 111, p. 186601, Oct 2013.

doi:10.6342/NTU202301896

[17] I. S. Grudinin, H. Lee, O. Painter, and K. J. Vahala, "Phonon laser action in a tunable two-level system," *Phys. Rev. Lett.*, vol. 104, p. 083901, Feb 2010.

[18] R. P. Beardsley, A. V. Akimov, M. Henini, and A. J. Kent, "Coherent terahertz sound amplification and spectral line narrowing in a stark ladder superlattice," *Phys. Rev. Lett.*, vol. 104, p. 085501, Feb 2010.

[19] I. Mahboob, K. Nishiguchi, A. Fujiwara, and H. Yamaguchi, "Phonon lasing in an electromechanical resonator," *Phys. Rev. Lett.*, vol. 110, p. 127202, Mar 2013.

[20] U. Kemiktarak, M. Durand, M. Metcalfe, and J. Lawall, "Mode competition and anomalous cooling in a multimode phonon laser," *Phys. Rev. Lett.*, vol. 113, p. 030802, Jul 2014.

[21] H. Jing, S. K. Özdemir, X.-Y. Lü, J. Zhang, L. Yang, and F. Nori, "$\mathcal{PT}$-symmetric phonon laser," *Phys. Rev. Lett.*, vol. 113, p. 053604, Jul 2014.

[22] J. Zhang, B. Peng, Ş. K. Özdemir, K. Pichler, D. O. Krimer, G. Zhao, F. Nori, Y.-x. Liu, S. Rotter, and L. Yang, "A phonon laser operating at an exceptional point," *Nature Photonics*, vol. 12, pp. 479–484, Aug 2018.

[23] Y. Jiang, S. Maayani, T. Carmon, F. Nori, and H. Jing, "Nonreciprocal phonon laser," *Phys. Rev. Applied*, vol. 10, p. 064037, Dec 2018.

[24] R. M. Pettit, W. Ge, P. Kumar, D. R. Luntz-Martin, J. T. Schultz, L. P. Neukirch, M. Bhattacharya, and A. N. Vamivakas, "An optical tweezer phonon laser," *Nature Photonics*, vol. 13, pp. 402–405, Jun 2019.

[25] J. Sheng, X. Wei, C. Yang, and H. Wu, "Self-organized synchronization of phonon lasers," *Phys. Rev. Lett.*, vol. 124, p. 053604, Feb 2020.

[26] J. B. Khurgin, M. W. Pruessner, T. H. Stievater, and W. S. Rabinovich, "Laser-rate-equation description of optomechanical oscillators," *Phys. Rev. Lett.*, vol. 108, p. 223904, May 2012.

doi:10.6342/NTU202301896

[27] S. Earnshaw, "On the nature of the molecular forces which regulate the constitution of the luminferous ether," *Transactions of the Cambridge Philosophical Society*, vol. 7, pp. 97–112, 1842.

[28] W. T. Scott, "Who was earnshaw?," *American Journal of Physics*, vol. 27, pp. 418–419, sep 1959.

[29] W. Paul, "Electromagnetic traps for charged and neutral particles," *Reviews of Modern Physics*, vol. 62, pp. 531–540, jul 1990.

[30] S. Seidelin, J. Chiaverini, R. Reichle, J. Bollinger, D. Leibfried, J. Britton, J. Wesenberg, R. Blakestad, R. Epstein, D. Hume, W. Itano, J. Jost, C. Langer, R. Ozeri, N. Shiga, and D. Wineland, "Microfabricated surface-electrode ion trap for scalable quantum information processing," *Physical Review Letters*, vol. 96, p. 253003, jun 2006.

[31] D. James, "Quantum dynamics of cold trapped ions with application to quantum computation," *Applied Physics B: Lasers and Optics*, vol. 66, pp. 181–190, feb 1998.

[32] S.-L. Zhu, C. Monroe, and L.-M. Duan, "Trapped ion quantum computation with transverse phonon modes," *Phys. Rev. Lett.*, vol. 97, p. 050505, Aug 2006.

[33] A. Ashkin, "Acceleration and trapping of particles by radiation pressure," *Physical Review Letters*, vol. 24, pp. 156–159, jan 1970.

[34] R. Grimm, M. WeidemÃijller, and Y. B. Ovchinnikov, "Optical dipole traps for neutral atoms," in *Advances In Atomic, Molecular, and Optical Physics*, pp. 95–170, Elsevier, 2000.

[35] A. Einstein, "Zur quantentheorie der strahlu10.1038/187493a0ng," *Physikalische Zeitschrift*, vol. XVIII, pp. 121–128, 1917.

[36] T. H. MAIMAN, "Stimulated optical radiation in ruby," *Nature*, vol. 187, pp. 493–494, aug 1960.

[37] O. Svelto, *Principles of Lasers*. Springer, 2007.

doi:10.6342/NTU202301896

[38] C. Raman, "A new radiation," *Indian J. Phys.*, vol. 2, pp. 38710.1088/1464–4266/2/3/201, 1927.

[39] "Correspondence," *Proceedings of the IRE*, vol. 50, no. 11, pp. 2365–2383, 1962.

[40] G. Eckhardt, R. W. Hellwarth, F. J. McClung, S. E. Schwarz, D. Weiner, and E. J. Woodbury, "Stimulated raman scattering from organic liquids," *Physical Review Letters*, vol. 9, pp. 455–457, dec 1962.

[41] J. Mompart and R. Corbalán, "Lasing without inversion," *Journal of Optics B: Quantum and Semiclassical Optics*, vol. 2, pp. R7–R24, may 2000.

[42] Y. R. Shen and N. Bloembergen, "Theory of stimulated brillouin and raman scattering," *Physical Review*, vol. 137, pp. A1787–A1805, mar 1965.

[43] W. E. Lamb, "Theory of an optical maser," *Phys. Rev.*, vol. 134, pp. A1429–A1450, Jun 1964.

[44] D. Wineland, C. Monroe, W. Itano, D. Leibfried, B. King, and D. Meekhof, "Experimental issues in coherent quantum-state manipulation of trapped atomic ions," *Journal of Research of the National Institute of Standards and Technology*, vol. 103, p. 259, may 1998.

[45] J. Eschner, G. Morigi, F. Schmidt-Kaler, and R. Blatt, "Laser cooling of trapped ions," *Journal of the Optical Society of America B*, vol. 20, p. 1003, may 2003.

[46] G. Morigi, J. Eschner, and C. H. Keitel, "Ground state laser cooling using electromagnetically induced transparency," *Physical Review Letters*, vol. 85, pp. 4458–4461, nov 2000.

[47] M. Orszag, *Quantum Optics*. Springer International Publishing, 2016.

[48] D. Kielpinski, C. Monroe, and D. J. Wineland, "Architecture for a large-scale ion-trap quantum computer," *Nature*, vol. 417, pp. 709–711, jun 2002.

doi:10.6342/NTU202301896

[49] R. B. Blakestad, C. Ospelkaus, A. P. VanDevender, J. H. Wesenberg, M. J. Biercuk, D. Leibfried, and D. J. Wineland, "Near-ground-state transport of trapped-ion qubits through a multidimensional array," *Physical Review A*, vol. 84, p. 032314, sep 2011.

[50] D. L. Moehring, C. Highstrete, D. Stick, K. M. Fortier, R. Haltli, C. Tigges, and M. G. Blain, "Design, fabrication and experimental demonstration of junction surface ion traps," *New Journal of Physics*, vol. 13, p. 075018, jul 2011.

[51] L.-M. Duan, B. Blinov, D. Moehring, and C. Monroe, "Scalable trapped ion quantum computation with a probabilistic ion-photon mapping," *Quantum Information and Computation*, vol. 4, pp. 165–173, may 2004.

[52] L.-M. Duan and C. Monroe, "Colloquium: Quantum networks with trapped ions," *Reviews of Modern Physics*, vol. 82, pp. 1209–1224, apr 2010.

[53] J. I. Cirac and P. Zoller, "A scalable quantum computer with ions in an array of microtraps," *Nature*, vol. 404, p. 579, Apr. 2000.

[54] A. K. Ratcliffe, R. L. Taylor, J. J. Hope, and A. R. R. Carvalho, "Scaling trapped ion quantum computers using fast gates and microtraps," *Phys. Rev. Lett.*, vol. 120, p. 220501, May 2018.

[55] G.-D. Lin, S.-L. Zhu, R. Islam, K. Kim, M.-S. Chang, S. Korenblit, C. Monroe, and L.-M. Duan, "Large-scale quantum computation in an anharmonic linear ion trap," *EPL (Europhysics Letters)*, vol. 86, p. 60004, jun 2009.

[56] J. P. Home, D. Hanneke, J. D. Jost, D. Leibfried, and D. J. Wineland, "Normal modes of trapped ions in the presence of anharmonic trap potentials," *New Journal of Physics*, vol. 13, p. 073026, jul 2011.

[57] G. Pagano, P. W. Hess, H. B. Kaplan, W. L. Tan, P. Richerme, P. Becker, A. Kyprianidis, J. Zhang, E. Birckelbaw, M. R. Hernandez, Y. Wu, and C. Monroe, "Cryogenic trapped-ion system for large scale quantum simulation," *Quantum Science and Technology*, vol. 4, p. 014004, oct 2018.

doi:10.6342/NTU202301896

[58] J. J. García-Ripoll, P. Zoller, and J. I. Cirac, "Speed optimized two-qubit gates with laser coherent control techniques for ion trap quantum computing," *Physical Review Letters*, vol. 91, p. 157901, oct 2003.

[59] A. M. Steane, G. Imreh, J. P. Home, and D. Leibfried, "Pulsed force sequences for fast phase-insensitive quantum gates in trapped ions," *New Journal of Physics*, vol. 16, p. 053049, may 2014.

[60] C. D. B. Bentley, A. R. R. Carvalho, and J. J. Hope, "Trapped ion scaling with pulsed fast gates," *New Journal of Physics*, vol. 17, p. 103025, oct 2015.

[61] J. J. García-Ripoll, P. Zoller, and J. I. Cirac, "Coherent control of trapped ions using off-resonant lasers," *Physical Review A*, vol. 71, p. 062309, jun 2005.

[62] S.-L. Zhu, C. Monroe, and L.-M. Duan, "Arbitrary-speed quantum gates within large ion crystals through minimum control of laser beams," *Europhysics Letters (EPL)*, vol. 73, pp. 485–491, feb 2006.

[63] M. Palmero, S. Martínez-Garaot, D. Leibfried, D. J. Wineland, and J. G. Muga, "Fast phase gates with trapped ions," *Physical Review A*, vol. 95, p. 022328, feb 2017.

[64] T. Olsacher, L. Postler, P. Schindler, T. Monz, P. Zoller, and L. M. Sieberer, "Scalable and parallel tweezer gates for quantum computing with long ion strings," *PRX Quantum*, vol. 1, p. 020316, dec 2020.

[65] J. D. A. Espinoza, M. Mazzanti, K. Fouka, R. X. SchÃijssler, Z. Wu, P. Corboz, R. Gerritsma, and A. Safavi-Naini, "Engineering spin-spin interactions with optical tweezers in trapped ions," *Physical Review A*, vol. 104, p. 013302, jul 2021.

[66] Y. H. Teoh, M. Sajjan, Z. Sun, F. Rajabi, and R. Islam, "Manipulating phonons of a trapped-ion system using optical tweezers," *Physical Review A*, vol. 104, p. 022420, aug 2021.

doi:10.6342/NTU202301896

[67] L. Bond, L. Lenstra, R. Gerritsma, and A. Safavi-Naini, "Effect of micromotion and local stress in quantum simulations with trapped ions in optical tweezers," *Physical Review A*, vol. 106, p. 042612, oct 2022.

[68] M. Mazzanti, R. SchÃijssler, J. A. Espinoza, Z. Wu, R. Gerritsma, and A. Safavi-Naini, "Trapped ion quantum computing using optical tweezers and electric fields," *Physical Review Letters*, vol. 127, p. 260502, dec 2021.

[69] M. Mazzanti, R. Gerritsma, R. J. C. Spreeuw, and A. Safavi-Naini, "Trapped ion quantum computing using optical tweezers and the magnus effect," 2023.

[70] S. Saskin, J. T. Wilson, B. Grinkemeyer, and J. D. Thompson, "Narrow-line cooling and imaging of ytterbium atoms in an optical tweezer array," *Phys. Rev. Lett.*, vol. 122, p. 143002, Apr 2019.

[71] C.-Y. Lee, K.-T. Lin, and G.-D. Lin, "Prototype of a phonon laser with trapped ions," *Physical Review Research*, vol. 5, p. 023082, may 2023.

[72] S. Jain, J. Alonso, M. Grau, and J. P. Home, "Scalable arrays of micro-penning traps for quantum computing and simulation," *Phys. Rev. X*, vol. 10, p. 031027, Aug 2020.

[73] M. S. Pierre Meystre, *Elements of Quantum Optics*. Springer-Verlag Berlin Heidelberg, 2007.

doi:10.6342/NTU202301896